Liquid Flow in Unsaturated Fractured Welded Tuffs:

I. Field Investigations

Rohit Salve, Joseph S. Y. Wang and Christine Doughty

Earth Sciences Division

Lawrence Berkeley National Laboratory

This work has been supported by the Director, Office of Civilian Radioactive Waste Management, through Memorandum Purchase Order EA9013MC5X between TRW Environmental Safety Systems, Inc., and the Ernest Orlando Lawrence Berkeley National Laboratory for the Yucca Mountain Site Characterization Project under U.S. Department of Energy Contract No. DE-AC03-76SF00098.

Abstract

Wetting-front movement, flow-field evolution, and drainage of fracture flow paths were evaluated within the Topopah Spring welded tuff at Yucca Mountain, Nevada. Equipment and techniques were developed for *in situ* quantification of formation intake rates, flow velocities, seepage rates, and volumes of fracture flow paths. Localized injections of liquid into a low-permeability zone (LPZ) and a high-permeability zone (HPZ) along a borehole were detected in two boreholes ~0.6 m below the point of injection. For the LPZ tests, water did not seep into an excavated slot located 1.65 m below and the liquid-release rate under constant-head conditions was observed to steadily decrease by two orders of magnitude (from >30 to < 0.1 ml/minute). In the HPZ, liquid-release rates under constant-head conditions were significantly higher (~100 ml/minute) and did not exhibit a strong systematic decline. HPZ tests were also conducted under constant-flow conditions using rates between 5 and 69 ml/min. Water dripped into the slot within 3-7 minutes at high injection rates (~28 to ~100 ml/minute), in 1 hour at the low injection rate of 14 ml/minute and in 5 hours at the lowest rate of 5 ml/minute. Slot seepage rates showed intermittent responses and the percentage of injected water recovered in the slot increased as each test progressed, approaching steady-state values after ~10 liters of water had been injected. A maximum of 80% of the injected water was recovered during high-rate injection tests. The flow path volumes were found to increase from less than 0.2 liter to about 1.0 liter during the course of each HPZ test. The data collected during these field tests along with fracture network information, are used by *Doughty et al.* [this issue] to gain an conceptual understanding of liquid flow in unsaturated fractured welded tuff.

1. Introduction

A clear understanding of flow and transport in the unsaturated, fractured rock environment is essential for the development of Yucca Mountain as a potential geological repository of spent fuels and high-level nuclear waste. Recent observations related to flow of liquids at Yucca Mountain indicate that fractures can be primary flow paths in the unsaturated zone. A model that incorporates fracture-dominated flow conditions would be a strong departure from early conceptual models of matrix-dominated flow, which (based on capillary considerations) envisioned flow to occur primarily through the rock matrix under ambient unsaturated conditions [*Montazer and Wilson*, 1984; *Wang and Narasimhan*, 1985]. Such a shift in paradigm would have significant ramifications on repository design and performance [e.g., *Doughty and Pruess*, 1992].

Evidence for fracture-dominated flow is largely based on indirect field observations, including the presence of perched water bodies with apparent ages younger than water in the surrounding tuff matrix [*Pruess et al.*, 1999], water-associated mineral deposits on fracture surfaces [*Paces et al.*, 1996], and bomb-pulse ^{36}Cl signals detected at isolated locations within the mountain [*Fabryka-Martin et al.*, 1996]. Direct evidence of flow in fractures remains elusive, largely because of technical difficulties encountered in locating and measuring fracture flow underground.

Early conceptual models developed to describe flow through unsaturated fractures, with fractures and matrix explicitly taken into account [e.g., *Wang and Narasimhan*, 1985;

Pruess and Wang, 1987; *Pruess and Tsang*, 1990; *Nitao and Buscheck*, 1991], are based on the underlying premise of capillary equilibrium between fractures and matrix. Because capillary forces are much stronger in the matrix, mobile liquid will not exist anywhere in the fracture unless the surrounding matrix is nearly fully saturated, in which case the fracture will be locally saturated as well. Hence, unsaturated flow along the fracture plane depends strongly on the continuity of locally saturated aperture segments. *Pruess* [1999] argues for a rather different scenario, with water flowing freely in networks of interconnected fractures while the surrounding matrix remains unsaturated. Another alternative view presented by *Tokunaga and Wan* [1997] suggests that significant water flux could occur as film flow in unsaturated fractures, with heterogeneities in both the fracture aperture distribution and the surface roughness controlling the fluid flow field. The wide divergence of the above models emphasizes the necessity of exploring fracture flow and fracture/matrix interactions *in situ*.

The fractured, welded rock formation in Yucca Mountain, which contains fractures of varying densities, orientations, spatial extents, and aperture/roughness distributions, poses experimental challenges with regard to instrument placement and sampling techniques [*Evans and Nicholson*, 1987]. While techniques developed for unconsolidated soils initially formed the basis for the characterization of unsaturated fractured rocks, new monitoring and testing techniques are required. Techniques are continuously being developed for vertical boreholes from the ground surface [*Montazer*, 1987; *Rousseau et al.*, 1994; *Hubbell and Sisson*, 1996; *Rousseau et al.*, 1997] and for horizontal boreholes in underground tunnels [*Salve et al.*, 2000].

This paper presents the results of a field investigation on fracture flow and fracture/matrix interactions in the Topopah Spring welded tuff rocks (TSw) at Yucca Mountain, using techniques developed specifically for *in situ* testing of flow in fractured rock. Numerical modeling studies done in conjunction with the field tests are presented in a companion paper [*Doughty et al*, this issue]. The objective of this study was to estimate hydraulic parameters such as formation intake rates, flow velocities, seepage rates, and flow-path volumes under controlled boundary conditions. Field tests were designed to study the evolution of focused flow with localized releases because the release of contaminated fluid is likely to be localized either after waste-package failure or from transient high infiltration events. Under these conditions, the most practical procedure is to observe fracture flow, and then try to infer fracture/matrix interactions. Direct observation of fracture/matrix interactions can be done by using dyed liquid and mining back the rock after a liquid-release test, but this precludes repeating experiments under a range of boundary conditions.

2. Methods

Field experiments were conducted in fractured, welded tuff within Yucca Mountain over a period of six weeks starting in late July 1998. These experiments included multiple releases of tracer-laced water in one low-permeability zone (LPZ) and one high-permeability zone (HPZ) along an injection borehole. Permeabilities of these zones were determined from air-permeability measurements conducted over 0.3-m sections along the borehole. The measured air permeability was 2.7×10^{-13} m^2 and 6.7×10^{-12} m^2 for the

LPZ and HPZ respectively. During and following liquid release events, changes in saturation and water potential in the fractured rock were measured in three monitoring boreholes. These changes were continuously recorded by an automated data acquisition system. Water that seeped into the excavated slot below the injection zone was collected, quantified for volumes and rates, and analyzed for tracers.

2.1 The test bed

The test bed is located approximately ~210 m below the surface of the mountain in the Exploratory Studies Facility (ESF, see Figure 1a), within the middle nonlithophysal portion of the TSw. The rock is visibly fractured with predominantly vertical fractures and few subhorizontal fractures. Relatively wide fracture spacing (on the order of tens of centimeters) facilitated the choice of injection zones, allowing discrete fractures and well-characterized fracture networks to be isolated by packers for localized flow testing.

A horizontal slot and a series of horizontal boreholes are the distinct features of the test bed (Figure 1b). The slot, located below the test bed, was excavated by an over-coring method. The excavation sequence required first the drilling of parallel pilot holes, 0.10 m in diameter, over 4 m in length, with a 0.22-m spacing, normal to the alcove wall. The pilot holes were then over-cored by a 0.3-m drill-bit to excavate the 2.0-m-wide, 4.0-m-deep and 0.3-m-high slot located approximately 0.8 m above the alcove floor. Three I-beam supports were installed along the length of the slot for support. Four horizontal boreholes, 0.1 m in diameter and 6.0 m in length, were drilled perpendicular to the alcove wall above the slot. Boreholes A and B were located 1.6 m above the slot ceiling, while

boreholes C and D were 0.9 m and 1.0 m above the slot ceiling, respectively, and 0.7 m apart (Figure 1b).

Borehole A was used for fluid injection while boreholes B, C and D were monitored for changes in moisture conditions. The slot was used to collect water seeping from the fractured rocks above. A flexible plastic curtain 3.0 m wide and 0.9 m high was installed to cover the slot face and minimize air movement between the alcove and slot.

2.2 Instrumentation

There were three distinct components to the flow investigation: (1) controlled release of water into isolated zones, (2) borehole monitoring for changes in saturation and water potential, and (3) collection of seepage from the slot ceiling. Key features of new instruments developed for this field investigation are presented below.

2.2.1 Fluid Injection

The liquid release experiments required water to be injected into the formation over a 0.3-m zone in the borehole under constant-head or constant-rate conditions. The constant-head tests were conducted first to determine the maximum rates at which the zone could take in water. The subsequent set of experiments required that water be released to the formation at predetermined rates ranging from ~ 5 ml/min to ~ 100 ml/min. Both the constant-head method and the constant-rate method of injection were incorporated in the fluid-release apparatus. The main components of the fluid release apparatus included an inflatable packer system for isolating the injection zone, a pump

for delivering water, and a reservoir for providing a continuous supply of water (Figure 2a).

The inflation packer system consisted of two rubber packers, each 0.60 m long, connected to an inflation line (Figure 2b). Two stainless tubes (0.95 cm and 0.31cm ID) passed through one of the packers to provide fluid (air and water) access into the injection zone. The 0.95-cm tube was used to deliver fluid into the injection zone, while the 0.31-cm tube was used as a siphon to remove excess water from the injection zone. Before liquid was released into the formation, the packer system was located to straddle the zone of interest (determined from air-permeability measurements) and then inflated to a pressure of ~ 200 kPa. The 0.95-cm ID stainless steel tube was then connected to a water supply line from a constant head or a constant-rate system. During the entire period of injection, pressure in the inflation packers was continuously monitored to ensure that the injection zone remained isolated from adjacent zones of the borehole.

To capture the temporal variability in the vertical flux of water from the injection zone, an automated liquid-release system was developed. This system allowed for continuous measurement of local liquid-release rates. The unit consisted of a water reservoir (~4.5 liters) for water supply to a clear acrylic constant-head chamber. The chamber, 0.25 m ID and 0.30 m tall, served to maintain a constant head of water above the liquid-release surface within the injection zone (Figure 2c). The hydraulic head was maintained with a level switch that activated the pump when the water level dropped below the control level. The control level was nominally set at or slightly above the elevation of the

horizontal injection borehole. Two pressure transducers located at the base of the reservoir continuously recorded the height of water. A pulse damper was installed between the pump and tank to reduce any pulsating effects (caused by the pump) from migrating to the storage tank and influencing the pressure readings.

The constant-rate injection system included all the components used in the constant-head system without the constant-head chamber. To allow for easy regulation of flow rates in the field, we calibrated the pump before field deployment to relate flow rates with displayed numbers on a 10-turn speed control. In the field, the speed control was set at the desired flow rate before the pump was activated. The actual flow rate was determined from transducers located at the base of the water reservoir. A data acquisition system was used to record changes in head of water in the reservoir.

2.2.2 Borehole Monitoring

In three monitoring boreholes (B, C and D in Figure 1b), relative changes in saturation and water potential were measured continuously during the entire field investigation. Changes in resistance were measured with electrical resistivity probes (ERPs) [*Salve et al.*, 2000]. Water-potential measurements were made with psychrometers. Using the multiplexing capabilities of the data logger [model CR7, *Campbell Scientific Inc.*], hourly measurements of up to 80 psychrometers [model PST-55, *Wescor Inc.*] were automated. The chromel-constantan junction in the psychrometer was cooled with an electric current to a temperature below dew point to induce condensation, followed by evaporation without electric current. The temperature depression resulting from evaporation was recorded and used to determine water potentials in the vicinity of the psychrometers.

The psychrometers and ERPs were housed in Borehole Sensor Trays (BSTs) installed along the length of each monitoring borehole (Figure 3a). On each tray, psychrometers were installed at 0.5-m intervals along the borehole while ERPs were located at 0.25-m intervals (Figure 3b and 3c) The BSTs permitted direct contact between ERPs and the borehole wall. The psychrometers were installed inside small cavities (0.005 m in diameter) perforated through the BST wall to measure water potentials of the rock. A steel spoon, 3.0 m long with the same configuration as the trays, was used to guide each BST to the assigned location along the borehole. Two BSTs were located along each section of borehole, one in contact with the top of the borehole and the other with the bottom. Each pair of BSTs was separated by a wedge, which pressed the BSTs tight against the borehole wall.

2.2.3. Seepage Collection

To measure water seeping into the slot following liquid release into the injection borehole, we designed a water collection system to capture seepage from the slot ceiling (Figure 4). Design of this system was dictated by the slot geometry and locations of 'I' beam supports. A row of stainless steel trays was fabricated for each of the four accessible compartments between the I-beams. Each tray was an inverted pyramid 0.46 m long and 0.40 m wide and tapered to a single point 0.20 m from the top. For each compartment, seven trays were assembled along a single steel frame, allowing for easy installation inside the slot. A total of 28 collection trays were used during the tests. Water captured in the stainless steel trays was transferred into clear PVC collection bottles (0.076 m ID, 0.45 m tall). Water falling onto the trays was drained to the collection

bottles through Teflon tubes (0.635 cm OD). An intermittent vacuum was applied to the collection bottles such that water stored on the trays or in Teflon tubes could be sucked into the collection bottles.

2.3. Liquid-Release Experiments

Air-permeability measurements were conducted along 0.3-m sections of the injection borehole. The most and least permeable intervals were identified as the LPZ (0.75-1.05 m from the collar)and the HPZ (2.3-2.6 m from the collar). In both the LPZ and the HPZ, a series of constant-head tests was conducted to determine the temporal changes in the rate at which the formation could take in water. In the HPZ a second series of tests was conducted with different prescribed injection rates. Tests conducted in this field investigation are summarized in Table 1. The seepage rates into the slot were monitored during all tests.

All water used in the ESF was spiked with lithium bromide for tunnel mining-related activities and for most of the scientific investigations. Additional tracers were added to the water injected into the LPZ and during the first set of experiments in the HPZ (Table 1). During the tests, water that seeped into the slot was periodically sampled and analyzed for tracer concentrations.

Water was released into the LPZ three times over a period of two weeks, starting on 7/23/98 (Table 1). For the first event, water was injected at a constant flow rate of ~56 ml/min. At 66 minutes, water was observed in the overflow line, indicating that water

was being injected at a rate higher than the intake capacity of the zone. At this time, the flow rate on the pump was immediately reduced to ~6.0 ml/min. Within 22 minutes return flow ceased, and water was injected continuously at this rate for the next 4 hours and 23 minutes. During this injection, a total of 6.3 liters of water was injected into the zone, of which 0.7 liters was recovered as return flow. The other 5.6 liters was released into the formation. The average net release rate into the formation rate was 16 ml/min.

For the second liquid release in the LPZ, the constant-head injection system was used. The constant-head chamber was located adjacent to the injection borehole such that the head of water was 0.07 m in the injection zone. This constant head was maintained for 4 hours while the water level in the reservoir was continuously monitored. At the end of this constant-head period, water supply to the injection zone was discontinued, resulting in a falling-head boundary condition that lasted about 1 day. In total, 15 liters of water were introduced into the LPZ during the constant-head and falling-head periods.

The final release into the LPZ was initiated on 7/29/98, when water was introduced into the formation under a constant head maintained for 43 hours, after which ponded water in the injection zone continued to percolate into the formation under a falling head for 4 days. During the test, 1.0 liters of water were released under the constant-head boundary and 1.2 liters were released under the falling head.

In summary, 9.2 liters of water were released to the formation under a combination of constant- and falling-head boundary conditions in the LPZ.

Water was injected into the HPZ during two groups of tests over a period of two weeks (Table 1). The first group of four tests was conducted during 8/4-6/98; the second group was conducted during 8/25-27/98. The first two tests in the first group were constant-head tests that served to establish the intake rates at which the injection zone could release water to the formation. The first constant-head test had an average rate of ~119 ml/min, the second rate was ~98 ml/min. During the third test, conducted the next day, water was injected at approximately half the intake rates observed with the constant-head system (i.e. ~53 ml/min). During the fourth test on 8/6/98, water was injected at a constant rate of ~5 ml/min over 12 hours. During the second group of tests (over a period of four days starting on 8/25/98), the injection rate was sequentially reduced from 69, 38, 29, and finally to 14 ml/min.

3. Observations

Water released in the injection borehole flowed through the fractured rock and, in the case of the HPZ, some of the water seeped into the slot located 1.6 m below. Liquid-release rates in the injection zone were measured, saturation and water potential changes were observed along monitoring boreholes, and water seeping into the slot was collected.

3.1 Liquid Release Rates

Measurements of liquid release rates in the LPZ of the test bed exhibited a response similar to that observed for soils. The initially high rates asymptotically approached low steady-state values of ~0.35 ml/min (Figure 5a). Near continuity was observed in the

decreasing liquid-release rates even with a five-day gap between liquid releases into the formation (Figure 5b).

For the first two constant-head tests conducted in the HPZ, the rates of liquid release varied significantly during and between tests (Figure 6). In the first test, the liquid release rate climbed for the first sixty minutes and then remained steady for the next 15 minutes before briefly increasing sharply. For the remainder of the test, the rate fluctuated between 70 and 160 ml/min. In the second test, the liquid-release rate rapidly increased for the first 15 minutes. The rate then slowly decreased and leveled off near ~100 ml/min. Ninety minutes into the test, the liquid release rate briefly fell to 35 ml/min, sharply increased to 130 ml/min, and then slowly dropped down to a quasi-steady rate of 90 ml/min in the next 80 minutes.

3.2 Formation wetting and drying

During the LPZ tests, changes in saturation were detected by both the ERPs (Figure 7a and c) and psychrometers (Figure 7b and d) in the monitoring boreholes C and D in response to liquid releases located 0.75-1.05 m from the borehole collar of injection borehole A. No response was detected in borehole B. In both boreholes C and D, large changes in saturation were detected by either or both ERPs and psychrometers located between 0.9 and 1.9 m from the collar. At a distance of 2.15 m from the borehole collar, the changes were much smaller.

The wetting process reduces electrical resistance and increases the water potential (i.e., makes it less negative). The drying process induces the opposite effect. In borehole C, the first response to test LPZ-1 was detected by the ERP located at 0.90 m from the borehole collar, as illustrated in Figure 7a. A step increase in resistance was observed 30 minutes after water had been released, suggesting some initial drying with dry air preceding a wetting front. Two hours later, an abrupt increase in wetting was indicated by a stepped decrease in resistance. ERPs located at 1.15 and 1.65 m also detected the arrival of a wetting front within 2 to 4 hours of liquid release. In borehole D (Figure 7c) the ERPs located at 0.9 m from the collar were first to detect increases in saturation 30 minutes after the first release of water. At distances of 1.40 and 1.65 m, the wetting front arrived 6 hours later.

The borehole C psychrometer data in Figure 7b support the ERP data in Figure 7a with smoother and more systematic changes induced by wetting front arrivals. The sensors closer to the release point had larger changes in water potential. At distances between 1.40 and 2.15 m from the collar, water potentials were between -140 and -80 m before the first injection. Immediately after LPZ-1 began, water potentials began to rise, and they rose steadily for the next four days (during which LPZ-2 occurred), reaching values between -60 and -40 m. In response to the final injection period (i.e., LPZ-3, 7/29-8/4/98 in Table 1), the most noticeable increase in potential was observed in the psychrometer located at 1.40 m, where water potential increased from –140 to –15 m. In borehole D (Figure 7d) changes in water potential were observed between 0.90 and 2.15 m following tests LPZ-1 and LPZ-2. The extent of drying subsequent to these tests (as seen in the

decrease in water potentials at 1.40 and 1.65 m) was greater than observed in borehole C, and following LPZ-3 water potentials in this zone were similar to those observed following LPZ-2. The diurnal oscillations apparent in the middle 3 borehole D psychrometers (Figure 7d) indicate good communication with atmospheric pressure (i.e., a high-permeability connection to the drift. This is consistent with the more dynamic response to the water release events.

During the HPZ tests, changes in saturation were detected by both the ERPs (Figure 8a and c) and psychrometers (Figure 8b and d) in the monitoring boreholes from liquid releases located 2.30-2.60 m from the collar of injection borehole A. The zones between 2.15 and 2.40 m in borehole C and between 2.15 and 2.65 m in borehole D showed the largest changes during testing.

In borehole C changes in saturation were observed between 1.9 and 3.4 m from the borehole collar, with the largest changes observed between 2.15 and 3.15 m. (Both the ERPs and the psychrometers detected the changes.) The largest changes in water potentials were detected between 2.15 and 2.40 m from the borehole collar in borehole C, where pre-injection water potentials that were between -70 to -60 m climbed to between -30 and -10 m after the first set of releases. These values decreased slightly before increasing in response to the second set of releases. In borehole D, saturation changes were observed over a slightly wider span along the borehole (i.e., 1.65 to 3.65 m from the borehole collar), with the largest changes observed between 1.90 and 3.40 m from the borehole collar. Water potentials between locations 2.15 and 2.90 m increased over a

period of a week after the initial release of water in the HPZ and remained between -15 to -5 m for the duration of the second set of liquid releases. Interestingly, the borehole D psychrometer at 1.9 m showed no response to the liquid release events, but showed low potentials with a strong weekly variability, thus exhibiting good communication with the atmospheric pressure variations in the drift that reflect different conditions during the work week when the tunnel ventilation system is active and the quieter weekends.

In both boreholes, the ERP and psychrometer data suggest that after the first batch of water releases (i.e., 8/4-6/98), saturation significantly increased. At most borehole D sensor locations, this increase persisted until the start of the second period of injection (8/25-28/98), at which time more water was retained by the formation, resulting in further increases in saturation. In contrast, in borehole C, psychrometer and especially ERP data show that significant drying occurred in between the two series of tests.

3.3. Seepage into the slot

Seepage into the slot was observed during all eight tests in the HPZ. (Test results are summarized in Table 2.) The eight tests were conducted in two groups (see Table 1). During the first test in the first group (HPZ-1), water was first observed on the slot ceiling within five minutes, after 0.41 liters of water was released under constant-head conditions. In the second and third tests, water appeared in the slot within 3 minutes, after 0.17 and 0.14 liters, respectively, had been released. In the fourth test, water appeared in the slot after five hours, with 1.50 liters of water injected at a rate of 5 ml/min.

In the second group of tests, travel time for the first drop of water was 3 minutes, after 0.14 liters was injected at a rate of ~69 ml/min (HPZ-5). In the two subsequent tests, the arrival time of the wetting front was 7 minutes, after 0.26 and 0.20 liters of water were injected at a rate of 38 and 29 ml/min, respectively. In the final test, water first appeared in the slot after 68 minutes, with 0.90 liters injected into the formation at a rate of 14 ml/min.

Significant variability was observed in the slot seepage rate during and between HPZ tests (Figure 9a). Intermittent seepage behavior was observed during all the tests, in which the rhythmical response that developed early in the test persisted for the duration of the test. Similar unsteady seepage has been observed in laboratory experiments of fracture flow [e.g., *Persoff and Pruess*, 1995; *Glass et al.*, 1995, *Kneafsey and Pruess*, 1998; *Su et al.*, 1999]. Using parallel-plate experiments, *Su et al.* [1999] demonstrated that such cyclic behavior occurred when water flowed through a sequence of small to large to small aperture flow paths, which resulted in strong capillary forces periodically snapping threads of liquid.

Because of the variability in slot seepage rate, it is more convenient to compare the cumulative percentage of injected water that is recovered at the slot for the various HPZ tests (Figure 9b). This measure is a normalized integral of slot seepage rate. For a constant seepage rate, the cumulative percentage recovered would increase rapidly after the first drop of water arrived. The rate of increase would then smoothly decline until the cumulative percentage recovered reached a constant value (the ratio of the seepage rate to

the injection rate). This would occur when the total volume injected became large compared to the volume that had been injected when seepage into the slot began. For the most part, the cumulative percentages recovered shown in Figure 9b display these characteristics. An exception is test HPZ-1 (injection at 119 ml/min), in which the saw tooth cumulative percentage recovered suggests a strongly pulsed seepage rate. For most of the tests, the cumulative percentage recovered approached relatively constant values after approximately 10 liters of water had been injected. However, tests HPZ-4 and HPZ-8 were not run long enough to show a constant cumulative percentage recovered.

Figure 10 illustrates the distribution of seepage among the collection trays in the slot. During each test, water appeared on the slot ceiling at one single point below the injection zone. The spot could be identified by a rust spot approximately 0.05 m in diameter that developed on the I-beam separating trays 1-6 and 2-13. Seepage water was collected from four trays located around this localized point of entry. During these tests, water seeping into the slot was largely concentrated in a single tray, with the three other trays collecting significantly smaller amounts of water. Slight increases at higher injection rates were noticeable in some of the secondary trays. The remaining 24 trays stayed dry during all the liquid-release tests. A horizontal borehole located at the same height as the slot and approximately 1.0 m to its left was instrumented with ERPs and psychrometers that were monitored throughout the tests (Figure 1). None of the instruments showed evidence of water flow to the left of the slot, supporting the hypothesis that none of the injected water bypassed the slot.

In all the tests during which there was seepage, 0.5 to 1.3 liters of water entered the slot after water supply to the formation was switched off (Figure 11). Most of this water was collected within one hour, with recovery rates being largest immediately after the test. The constant-head test with ~98 ml/min release rate (HPZ-2) had a 'stepped' nature to the post-injection recovery. During the first fifteen minutes, the 0.8 liters of collected water appeared in four bursts, each containing 0.1-0.3 liters of water. Changes of similar magnitudes were observed in the tests with injection rates of ~53 ml/min (HPZ-3) and ~14 ml/min (HPZ-8).

3.4 Tracer Recovery

While none of the tracers introduced in LPZ was recovered, all tracers injected in the HPZ were detected in the water samples collected in the slot. Typically, tracers introduced in one test were rapidly flushed out of the system during the subsequent test (Figure 12). The pattern of recovered concentrations of tracers suggests that plug flow was the dominant process by which 'new' water replaced 'old' water from the previous test. Additionally, the recovered concentrations of potassium fluoride indicate that some initial retardation mechanism altered the behavior of the tracer during the early stages of injection. Some dissolution of tracers from the formation was observed during subsequent tests.

4. Summary And Discussion

The main objective of this paper is to present fracture flow data collected in a slotted test bed located in the TSw at Yucca Mountain. Because of the slot it was possible to

quantify flow both into and out of the test bed and better understand the nature of the flow field in the underground test facility. Test results revealed aspects of flow in unsaturated, fractured systems and provided insight towards the conceptualization of flow through unsaturated, fractured rock formations in which both fracture flow and fracture/matrix interactions play important roles.

Results from field tests indicate that the techniques developed to investigate flow in fractured, welded tuffs are effective for *in situ* characterization of certain fundamental flow parameters (such as travel times, percolation paths, and seepage rates, etc.). Additional automation and improvement are being developed to overcome the constraints on test design arising from limited access to the test bed that were encountered in the field studies.

The fluid-injection tests conducted in two zones within a single borehole at Yucca Mountain demonstrate the significant variability in the hydrologic responses. The formation response to liquid releases in the LPZ suggests a conceptual flow model consisting of a strongly heterogeneous fracture network in which the high-permeability fractures are not extensive or are poorly connected. The closed-end features tend to wet up early and remain saturated throughout the remainder of the test. The key features of the data supporting this model are 1) the large, decrease in injection rate (high-permeability closed-end fractures fill up first and thereafter do not participate; smaller interconnected fractures control the long-time injection rate); 2) the gradual responses of the monitoring borehole sensors, some of which monotonically reach steady state and

some of which show a dynamic response corresponding to closed-end and inter-connected fractures, respectively.; 3) the lack of through-flow to the slot (no long, inter-connected vertical fractures).

In contrast to the liquid-release rates observed in the LPZ, the HPZ did not show large decreases in release rates as additional water was introduced into the formation (Figure 6). Further, the rates fluctuated significantly during the entire duration of the liquid releases at constant head. Slot seepage rates also fluctuated strongly, whether liquid was injected under constant-head or constant-rate conditions. Flow between the injection interval and the underlying slot occurred quickly (1.6 m in 3 to 7 minutes) unless the injection rate was low. These features are consistent with a conceptual model dominated by high-conductivity, well-connected fracture flow paths. Furthermore, the localized water arrival at the slot suggests that flow predominantly occurred in a few preferential, channelized pathways, the 'fast flow paths' commonly associated with partially-saturated high-conductivity fractured rock [*Pruess*, 1999; *Pruess et al.*, 1999; *Su et al.*, 1999].

Generally, the monitoring borehole ERP and psychrometer responses were more abrupt for the HPZ tests than for the LPZ tests, consistent with the concept of a higher-conductivity, better-connected fracture network. Unfortunately, the ERP data, which shows sudden jumps suggestive of the kind of fluctuating, localized flow expected in fractured rock, also shows sudden jumps in resistivity that do not seem entirely plausible based on physical principles (e.g., simultaneous resistivity jumps at multiple sensors), making definitive inferences problematic. The relative locations of the HPZ injection

interval and the slot location where breakthrough was centered (tray 1-6) suggest that borehole C should have shown larger responses than borehole D (compare figures 1b and 10a). In fact, Figure 8 shows that although some of the largest saturation increases were noted in borehole D, the more dynamic responses were observed in borehole C, consistent with the notion of a through-going flow path there.

Volume estimates for water present in the vertical fast flow paths can be made from both early and late stages of the tests in the HPZ. Tests with relatively high injection rates (i.e., 29-100 ml/min) are particularly useful for estimating the volume of water occupying fast flow paths from early-stage data, because transit time between the injection interval and the slot is minimal, lessening the potential masking effects of lateral spreading, fracture/matrix interactions, and other capillary-driven flow. Here, the vertical flow-path volume between the injection zone and slot ceiling can be assumed to be the volume of water injected during each test before the arrival time of the first drop into the slot (Table 2). For the first test, when the test bed was undisturbed, this approach will over-estimate fast-path volume because it includes an additional loss to closed-ended fractures. An estimate of this loss is provided by the difference between the volume of water taken by the formation early in the first and second tests (i.e., 0.41-0.17 = 0.24 liters). Observations from the later tests suggest that the fracture-flow-path volume during the early stages of each test ranged between 0.14 and 0.26 liters.

A second estimate of the volume of vertical flow paths can be extracted from the postinjection seepage data (Figure 11) where the amount of water collected varied

between 0.5 and 1.3 liters for water released at rates between 14 and 69 ml/min. (Since postinjection seepage for the constant head injections included a finite volume of water from storage in the injection zone [~1.2 liters], the first two tests have been excluded in these estimates). While these volumes are significantly greater than estimates from the prior analysis of early transient data, they may underestimate vertical-flow-path volumes in situations where water is held up in fractures by capillary forces.

Our data indicate that between 60-80% of the injected water was recovered by the end of each of the high rate injection tests in the HPZ. With the test bed geometry and our conceptual model for flow arising from both the LPZ and HPZ tests, we are reasonably confident that the remaining 20-40% remained in the fractured rock formation, either held up by capillarity on the walls of the fast flow paths, trapped in high-permeability closed-end fractures, moving slowly through low-permeability connected fractures, or imbibed into the matrix. Numerical modeling of the LPZ and HPZ tests based on this conceptual flow model and an investigation of possible fast flow path geometries that would be consistent with the data are presented in a companion paper [*Doughty et al.*, this issue].

Acknowledgments

This work was supported by the Director, Office of Civilian Radioactive Waste Management, through Memorandum Purchase Order EA9013MC5X between TRW Environmental Safety Systems Inc. and the Ernest Orlando Lawrence Berkeley National Laboratory for the Yucca Mountain Site Characterization Project through U.S. Department of Energy Contract No. DE-AC03-76SF00098. Thanks are due to Robert Conroy, Paul Cook, John Dinsmoor, Jose Gonzales, Manuel Gonzales, Margaret Guell, Qinhong Hu, Lee Jacobs, Alan Mitchell, Gene Pokorny, Jan Stepak, Robert Terberg, Tetsu Tokunaga, and Robert Trautz for assistance in developing various aspects of the field experiments. Reviews of the manuscript by Peter Persoff, Tim Kneafsey and Dan Hawkes are gratefully acknowledged.

References

Doughty, C., R. Salve, and J. S. Y. Wang, Liquid flow in fractured Welded Tuffs: II Numerical Modeling, *Water Resour. Res.*, this issue, 2000.

Doughty, C. and K. Pruess, A similarity solution for two-phase water, air, and heat flow near a linear heat source in a porous medium, *Journal of Geophysical Res.*, 97, B2, 1821-1838, 1992.

Evans, D. D., and T. J. Nicholson, Flow and transport through unsaturated fractured rock: An overview, in *Flow and Transport through Unsaturated Fractured Rock*, edited by D. D. Evans and T. J. Nicholson, *Geophysical Monograph 42*, American Geophysical Union, Washington, D. C., 1987.

Fabryka-Martin, J. T., P. R. Dixon, S. Levy, B. Liu, H. J. Turin, and A. V. Wolfsburg, Summary report of Chlorine-36 studies: Systematic sampling for Chlorine-36 in the Exploratory Studies Facility, *Los Almos National Laboratory Milestone Report 3783AD*, Los Alamos National Laboratory, Los Alamos, New Mexico, 1996.

Glass, R. J., M. J. Nicholl, and V. C. Tidwell, Challenging models for flow in unsaturated, fractured rock through exploration of small scale processes, *Geophys. Res. Lett.*, *22*, 1457-1460, 1995.

Hubbell, J. N., and B. Sisson, Portable tensiometer use in deep boreholes, *Soil Science*, *161*(6), 377-381, 1996.

Kneafsey, T., and K. Pruess, Laboratory experiments on heat-driven two-phase flows in natural and artificial rock fractures, *Water Resour. Res.*, *34*, 1457-1460, 1998.

Montazer, P., Monitoring hydrologic conditions in the vadose zone in fractured rocks, Yucca Mountain, Nevada, in *Flow and Transport Through Unsaturated Fractured Rock*, edited by D. D. Evans and T. J. Nicholson, *Geophysical Monograph 42*, American Geophysical Union, Washington, D. C., 1987.

Montazer, P., and W.E. Wilson, Conceptual hyrologic model of low in the unsaturated zone, Yucca Mountain, Nevada, *U.S. Geol. Surv. Water Resour. Invest. Rep., 84-4355*, 1984.

Nitao, J., and T. Buscheck, Infiltration of a liquid front in an unsaturated, fractured porous medium, *Water Resour. Res.*, *27*, 2099-2112, 1991.

Paces, J. B., L. A. Newmark, B. D. Marshall, J. F. Whelan, and Z. E. Peterman, Ages and origins of subsurface secondary minerals in the Exploratory Studies Facility, *1996 Milestone Report 3GQH450M*, U.S. Geological Survey, Denver, Colorado, 1996.

Persoff, P., and K. Pruess, Two-phase flow visualization and relative permeability measurement in natural rough-walled rock fractures, *Water Resour. Res.*, *31*, 1175-1186, 1995.

Pruess, K., A mechanistic model for water seepage through thick unsaturated zones in fractured rocks of low matrix permeability, *Water Resources Res.*, 35, 4, 1039-1051, 1999.

Pruess, K., B. Faybishenko, G. S. Bodvarsson, Alternative concepts and approaches for modeling flow and transport in thick unsaturated zones of fractured rocks, *Journal Of Contaminant Hydrology, 38*(1-3), 281-322, 1999.

Pruess, K., and Y. W. Tsang, On two-phase relative permeability and capillary pressure of rough-walled rock fractures, *Water Resour. Res.*, *26*, 1915-1926, 1990.

Pruess, K., and J. S. Y. Wang, Numerical modeling of isothermal and nonisothermal flow in unsaturated fractured rock: A review, in *Flow and Transport Through Unsaturated Rock, Geophys. Monogr. Ser., vol. 42*, edited by D. D. Evans and T. J. Nicholson, pp. 11-21, AGU, Washington, D. C., 1987.

Rousseau, J. P., C. L. Loskot, F. Thamir, and N. Lu, Results of borehole monitoring in the unsaturated zone within the main drift area of the Exploratory Studies Facility, Yucca Mountain, Nevada, *Milestone SPH22M3*, U.S. Geological Survey, 1997.

Rousseau, J. P., M. Kurzmack, and A. Greengard, Results of prototype borehole instrumentation at the Hydrologic Research Facility, Area 25, NTS, *in A High-Level Radioactive Waste Management International Conference, 5th, Proceedings, Las Vegas, Nevada, May 22-26, 1994*, American Nuclear Society, La Grange, IL, 1994.

Salve, R., J. S. Y. Wang and T. K. Tokunaga, A probe for monitoring wetting front migrations in rocks, Submitted to *Water Resour. Res.*, 36, 1359-1367, 2000.

Su, G., J. T. Geller, K. Pruess, and F. Wen, Experimental studies of water seepage and intermittent flow in unsaturated, rough-walled fractures *Water Resour. Res., 35*, 1019-1037, 1999.

Tokunaga, T. K., and J. Wan, Water film flow along fracture surfaces of porous rock, *Water Resour. Res., 33*, 1287-1295, 1997.

Wang, J. S. Y., and T. N. Narasimhan, Hydrologic mechanisms governing fluid flow in a partially saturated, fractured, porous medium, *Water Resour. Res., 21*, 1861-1874,1985.

Figure Captions

Figure 1. Plan view of location (a) and vertical view of layout (b) of test bed within the ESF at Yucca Mountain. Figures are not drawn to scale.

Figure 2. Liquid-release system for constant-head and constant-rate injections.

Figure 3. Borehole monitoring system.

Figure 4. Water-collection system installed in slot.

Figure 5. Water intake rates observed in the low-permeability zone (LPZ).

Figure 6. Water intake rates observed in the high-permeability zone (HPZ).

Figure 7.Changes in electrical resistance and water potentials detected in boreholes 'C' and 'D' during liquid injection into the LPZ. Shaded zones indicate the location and duration of liquid-release events. Note resistance axis is inverted.

Figure 8. Changes in electrical resistance and water potentials detected in boreholes 'C' and 'D' during liquid injection into the HPZ. Shaded zones indicate the location and duration of liquid-release events. Note resistance axis is inverted.

Figure 9. Seepage into slot: (a) Seepage rates for various HPZ tests and (a) Cumulative percentage of injected water recovered.

Figure 10. Seepage into collection trays in the slot: (a) Tray configuration and (b) Final cumulative percentage of injected water recovered in different trays.

Figure 11. Volume of water recovered in the slot after liquid injection to the HPZ was stopped.

Figure 12. Tracer concentrations in seepage water following injection into the HPZ.

Table Captions

Table 1. Amount of Water and Types of Tracers Released into the Injection Borehole.

Table 2. Summary of Liquid Injection Tests in the High-Permeability Zone.

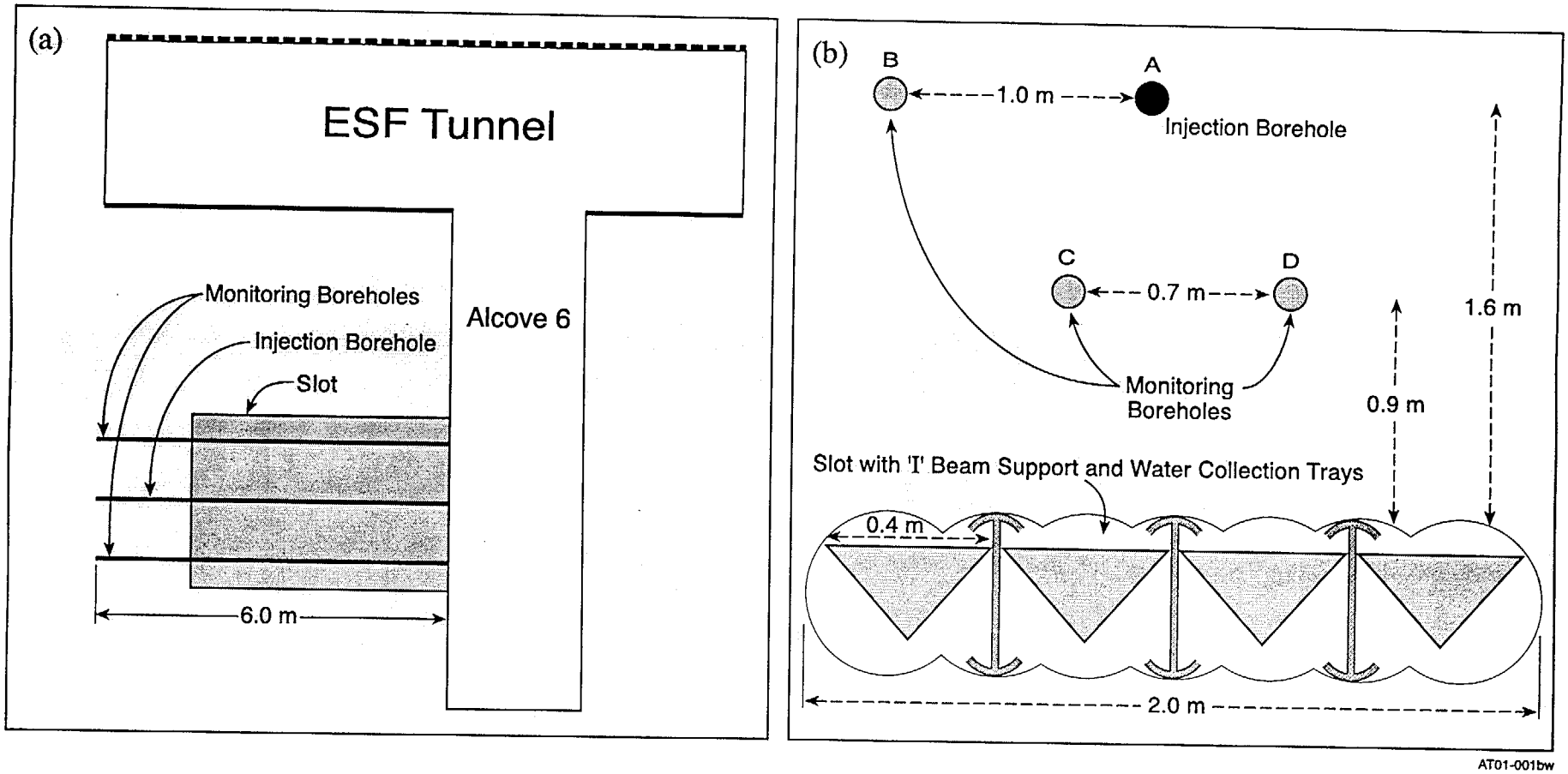

Figure 1. Plan view of location (a) and vertical view of layout (b) of test bed within the ESF at Yucca Mountain. Figures not drawn to scale.

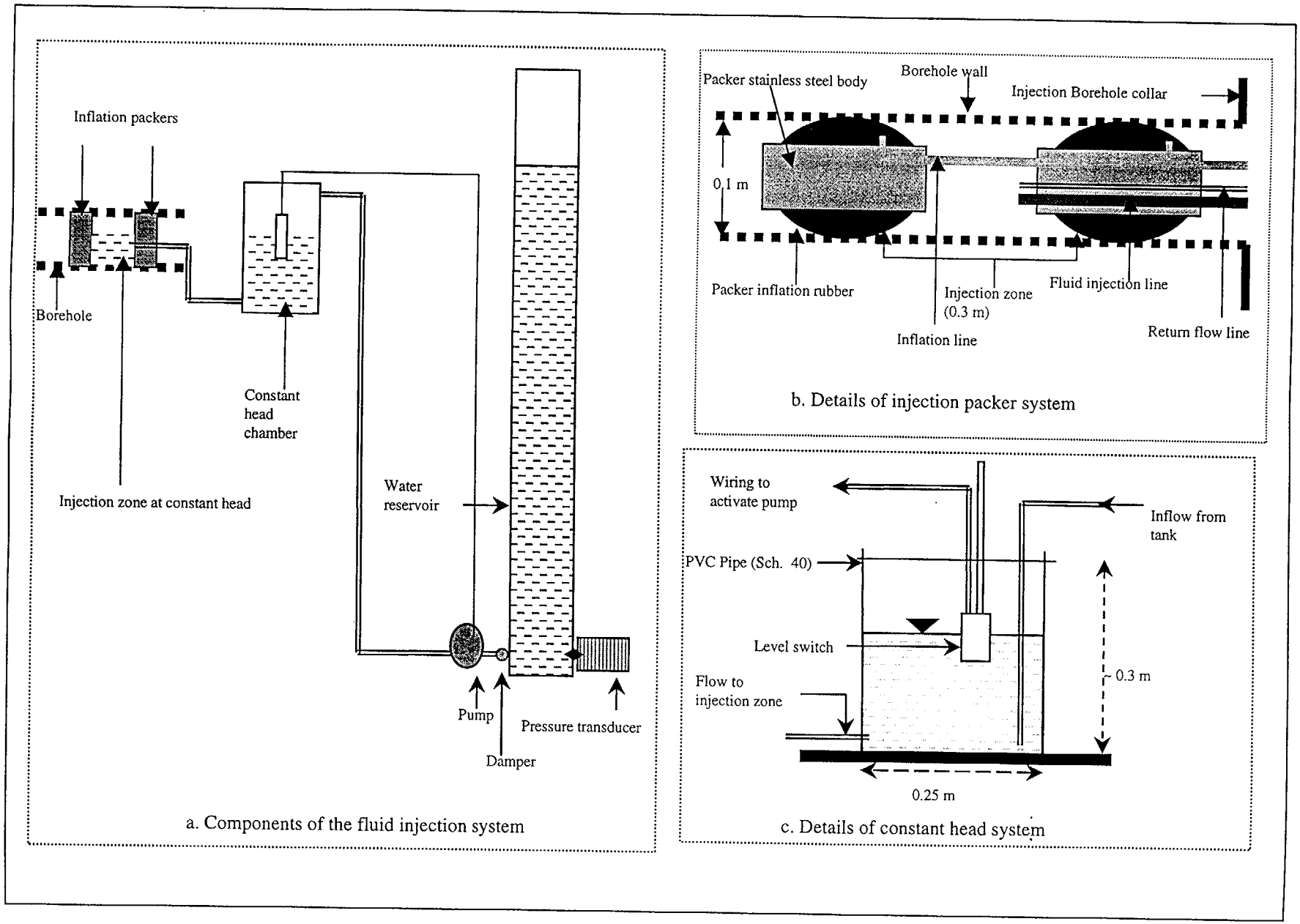

Figure 2. Liquid-release system for constant-head injections. For constant-rate injections the constant-head chamber is deactivated.

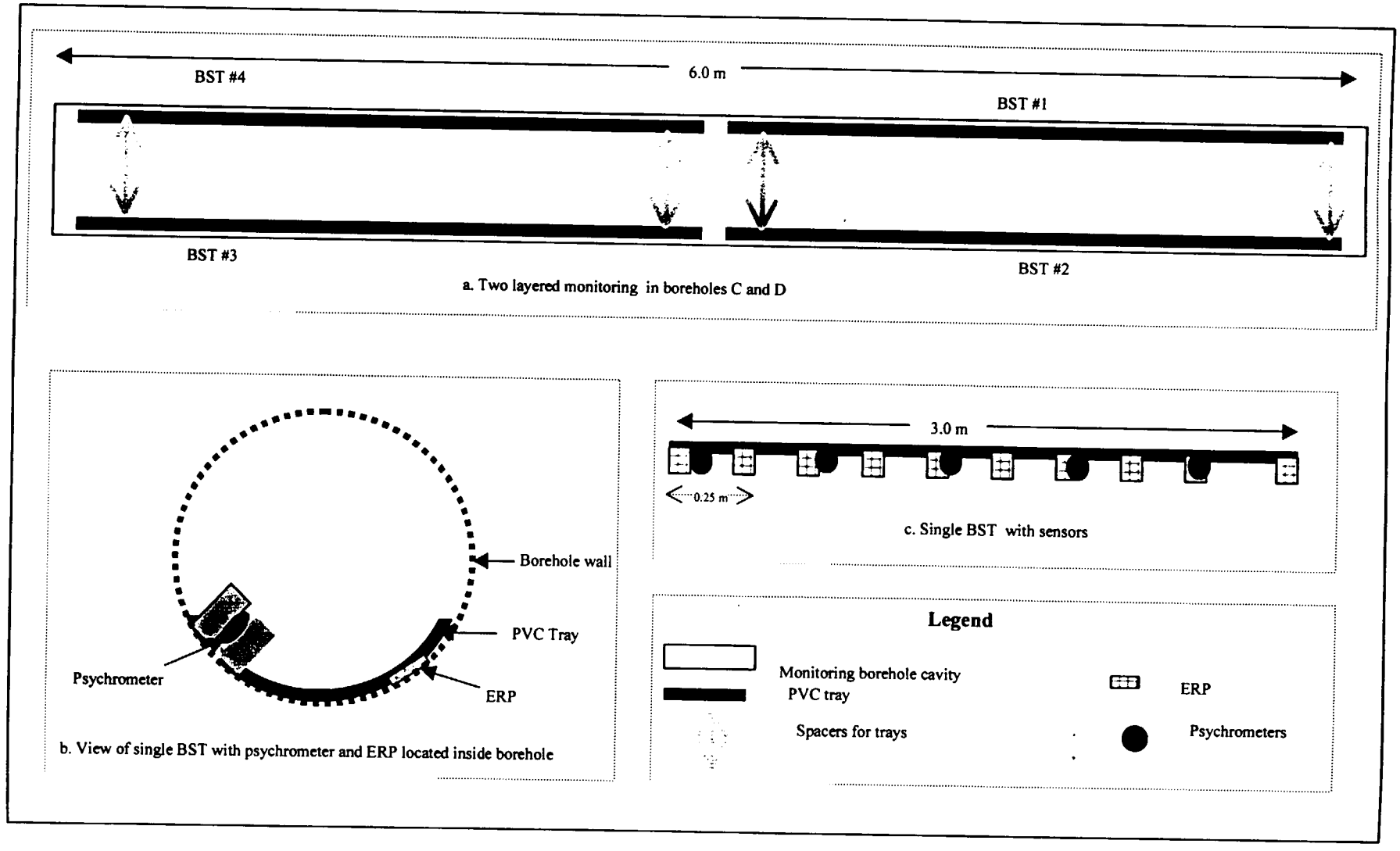

Figure 3. Borehole monitoring system.

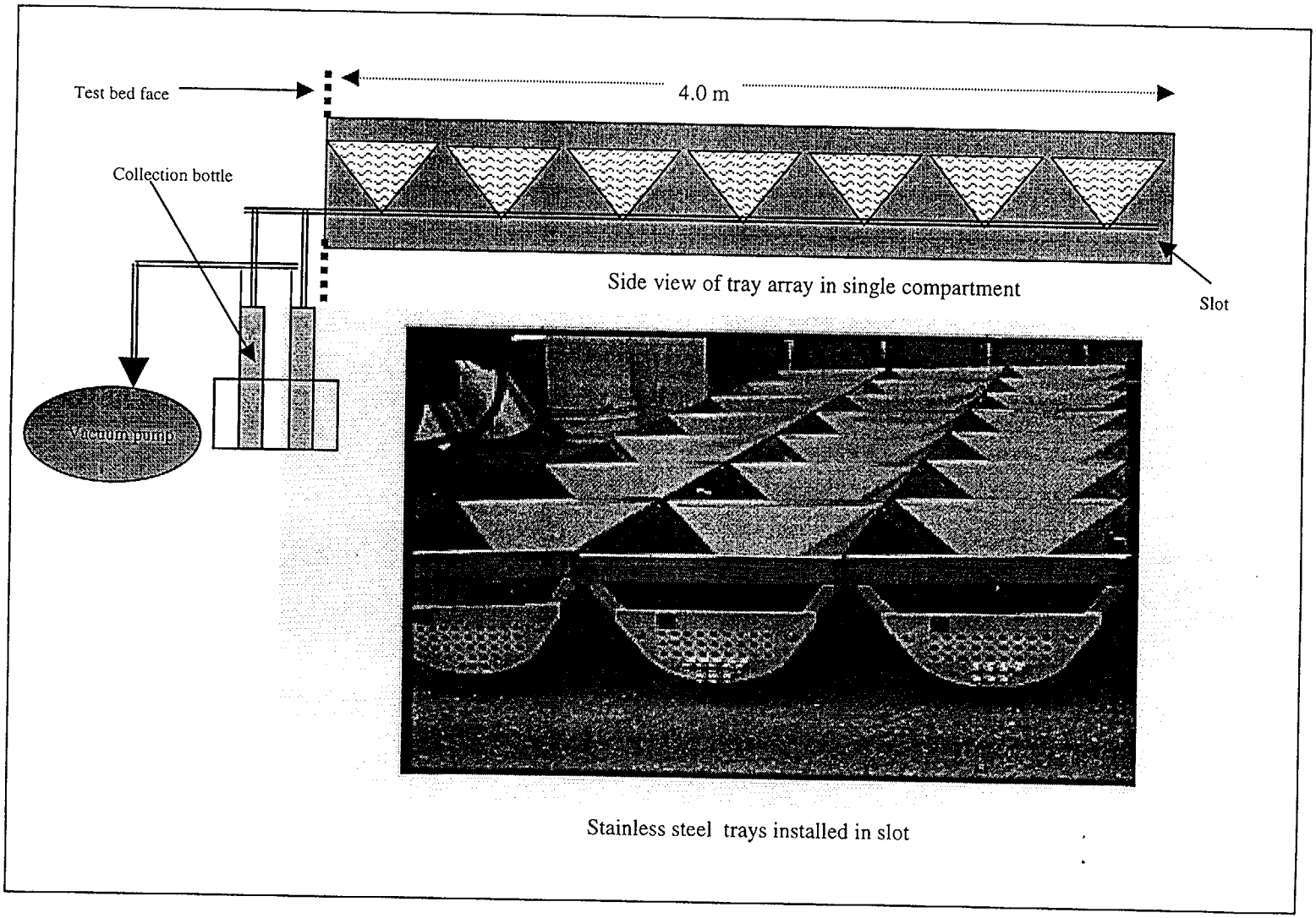

Figure 4. Water-collection system installed in slot.

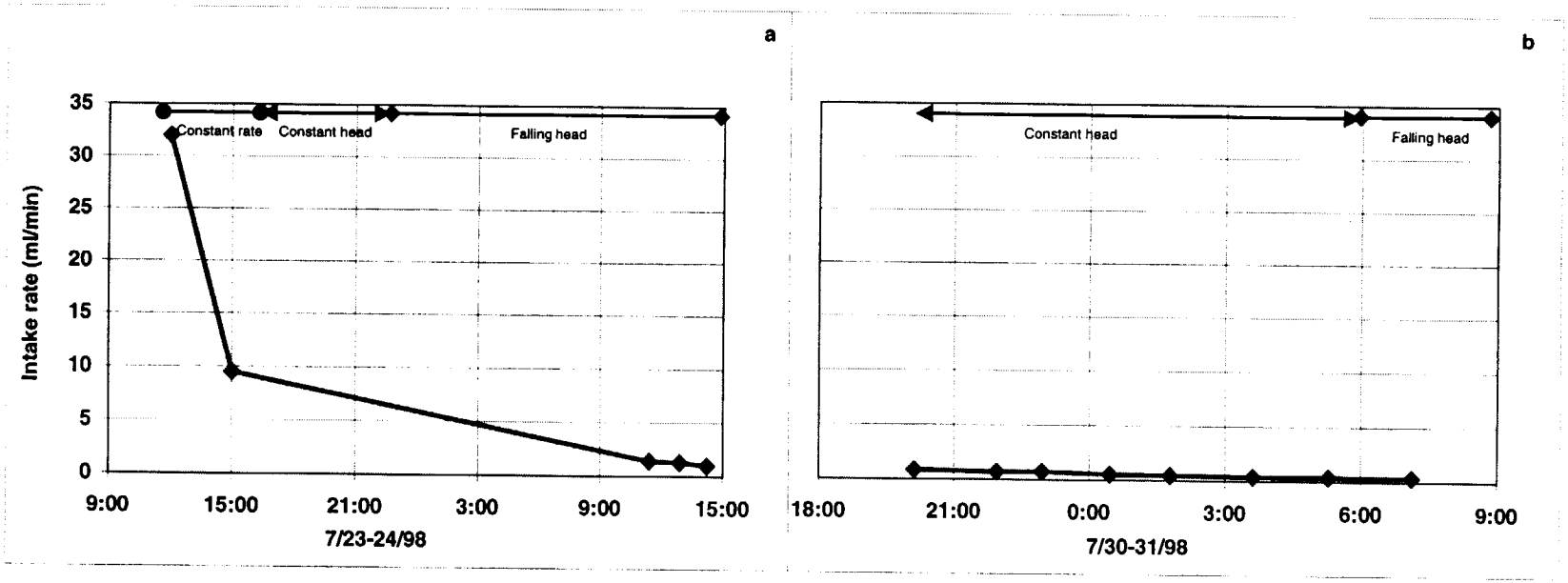

Figure 5. Water intake rates observed in the low-permeability zone (LPZ).

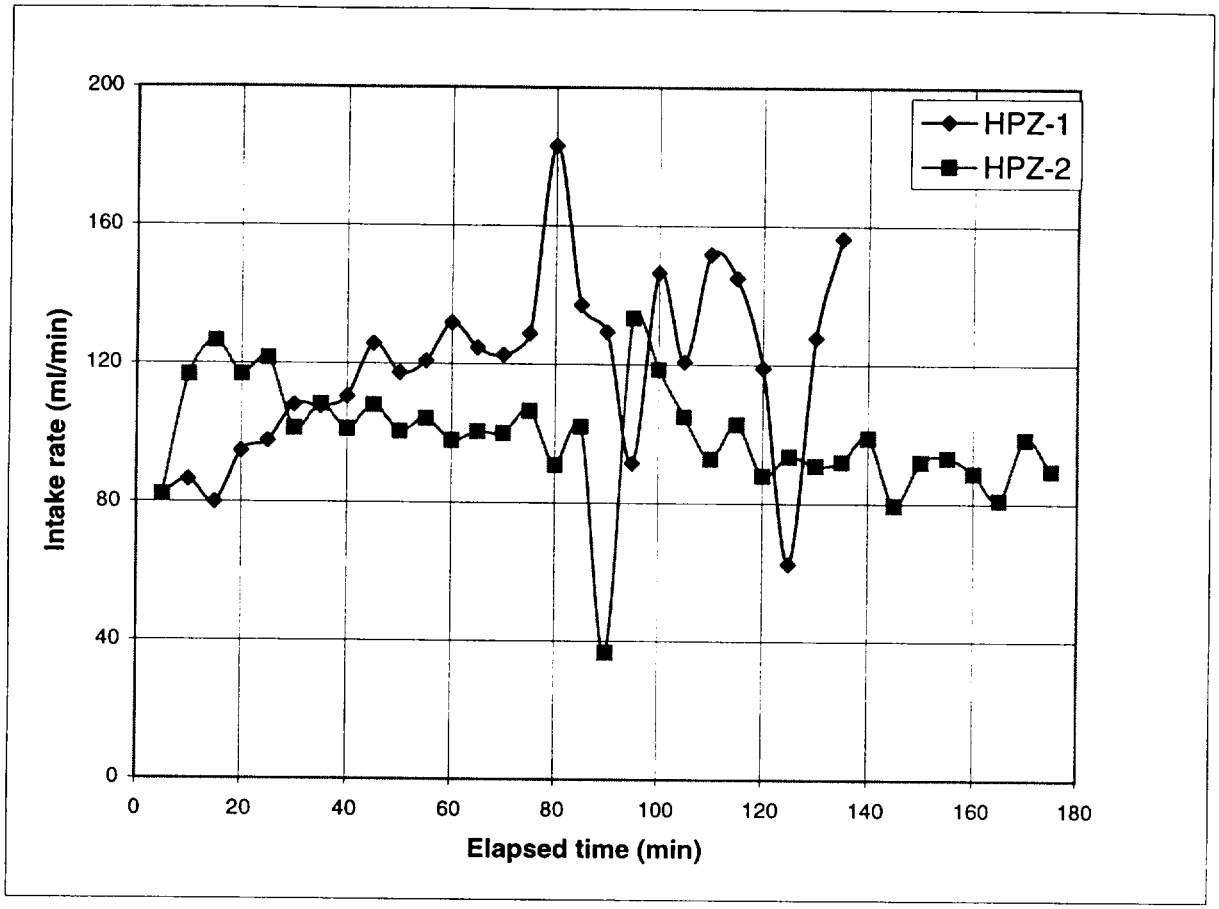

Figure 6. Water intake rates observed in the high-permeability zone (HPZ).

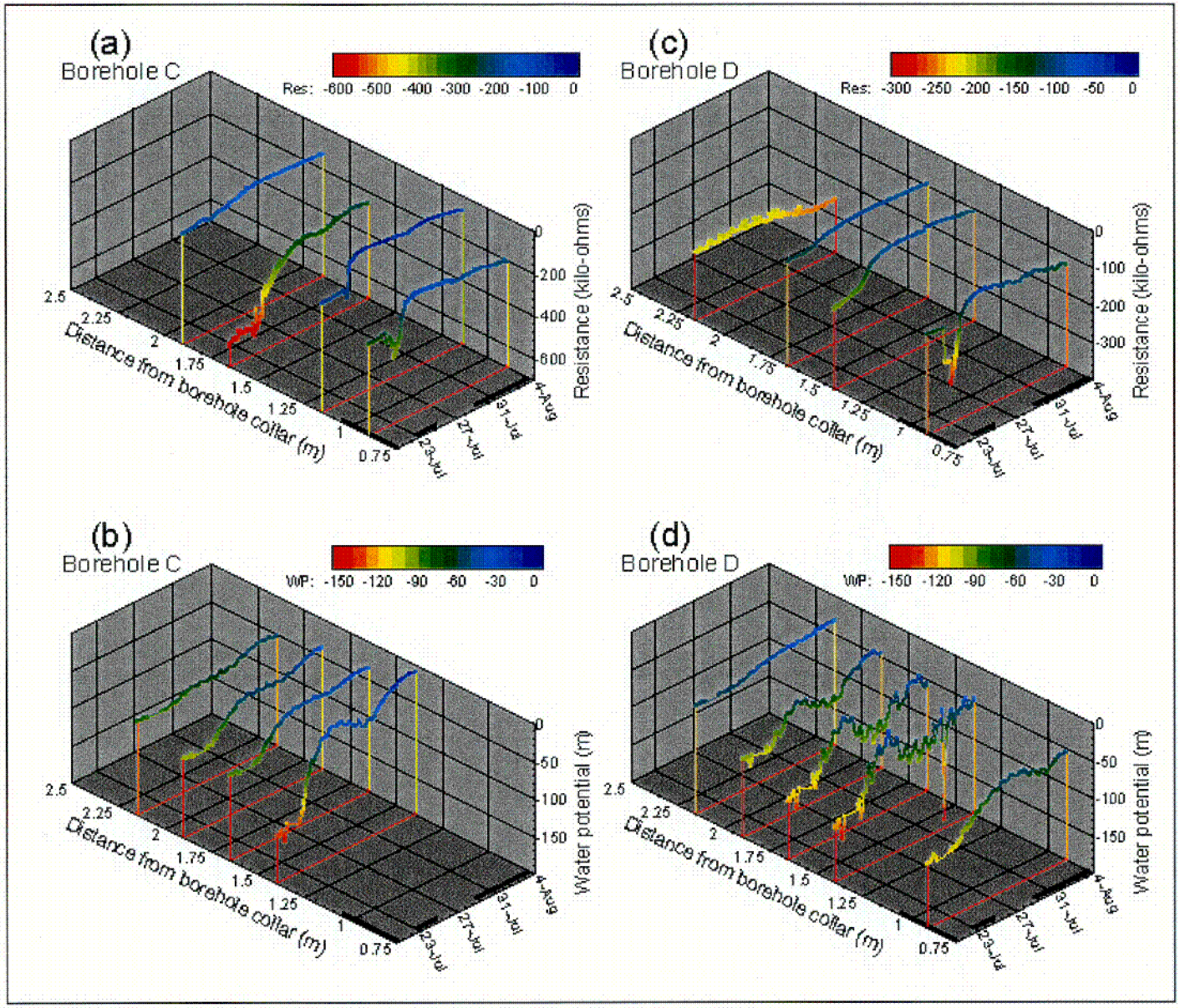

Figure 7. Changes in electrical resistance and water potentials detected in Borehole 'C' and 'D' during liquid injection into the LPZ. Dark lines along the time axis indicate the duration of liquid-release events. Note resistance axis is inverted.

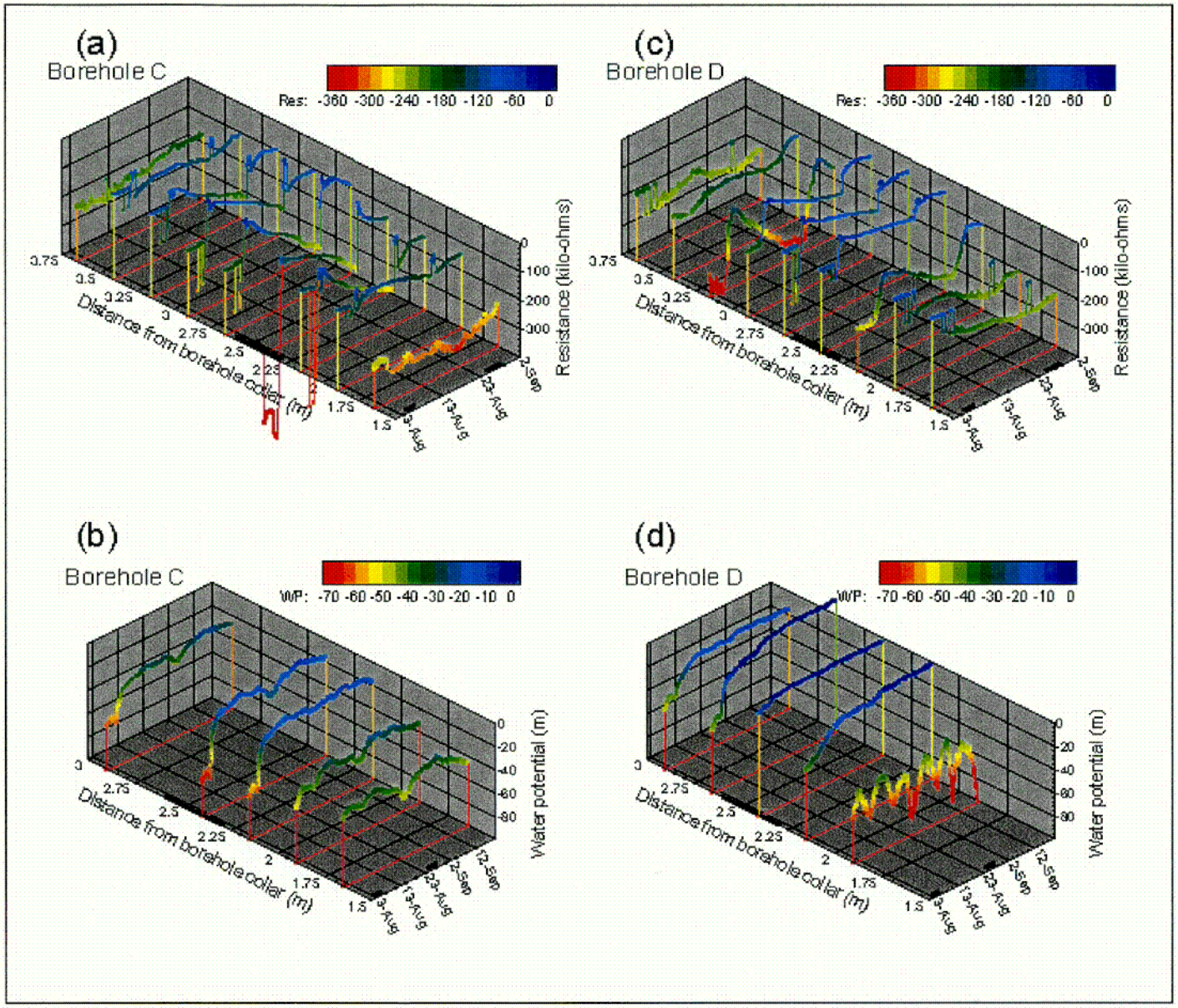

Figure 8. Changes in electrical resistance and water potentials detected in Borehole 'C' and 'D' during liquid injection into the HPZ. Dark lines along the time axis indicate the duration of liquid-release events. Note resistance axis is inverted.

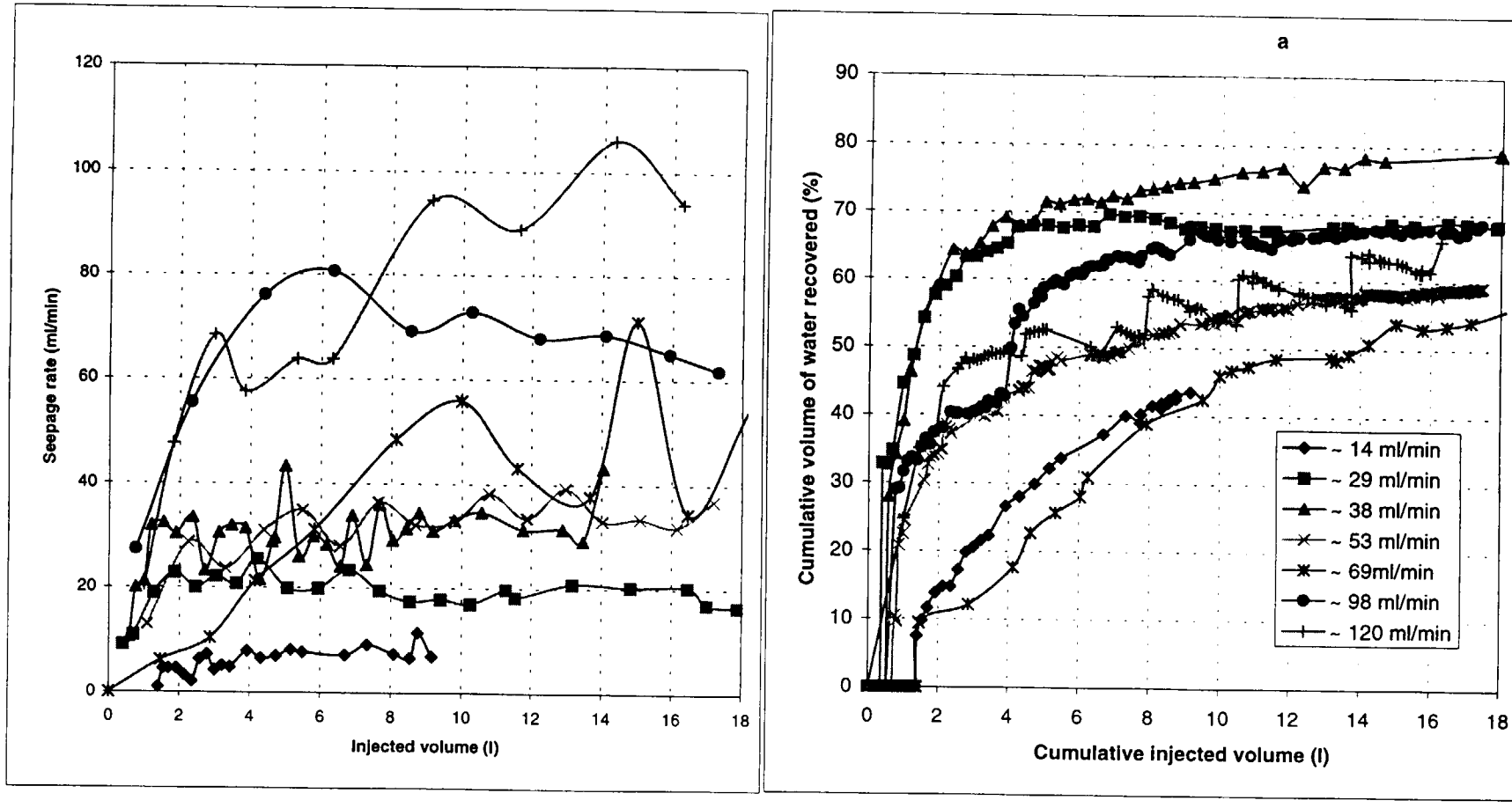

Figure 9. Seepage into slot: (a) Seepage rates for various release rates and (b) Cumulative percentage of injected water recovered .

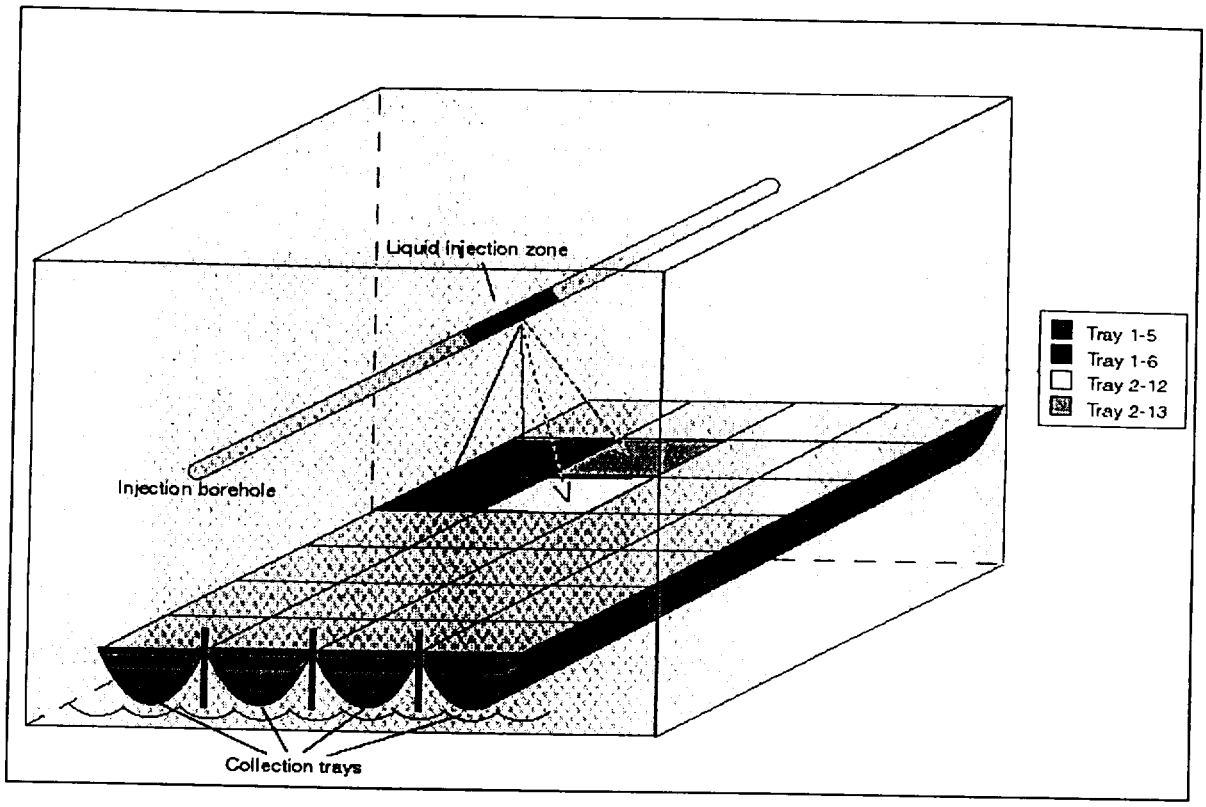

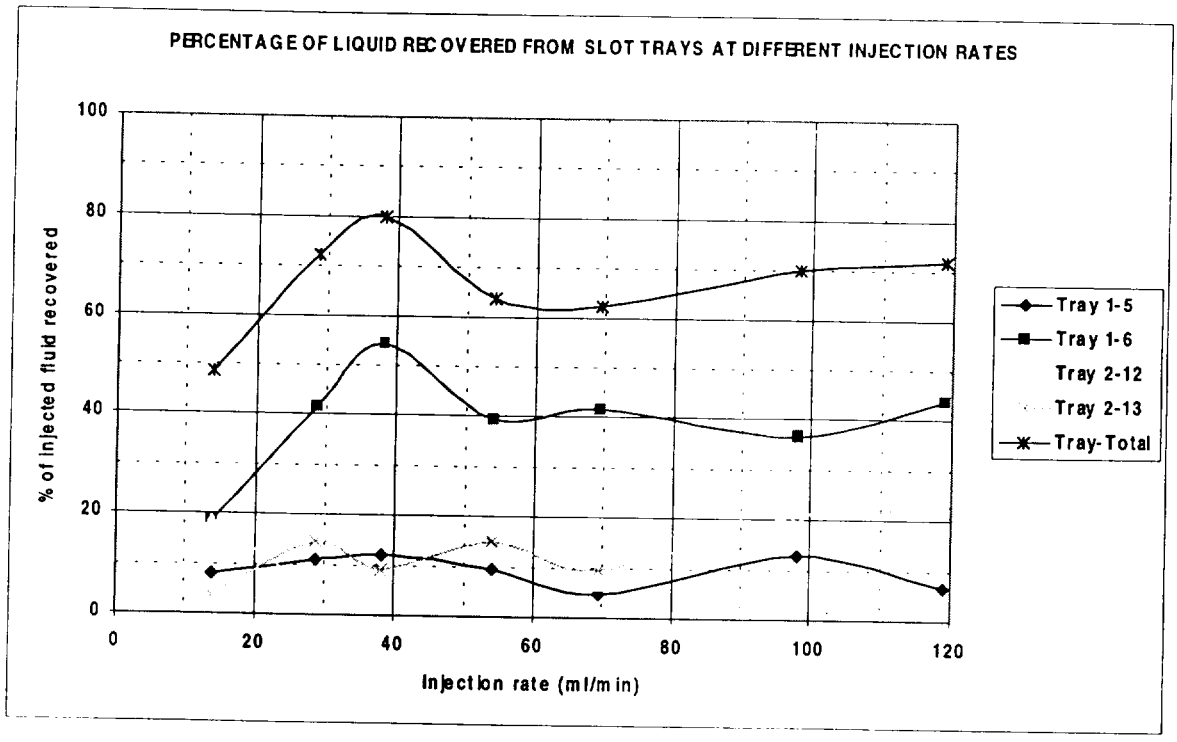

Figure 10. Seepage into collection trays in the slot: a. Tray configuration and b. Percentage of injected water recovered in different trays.

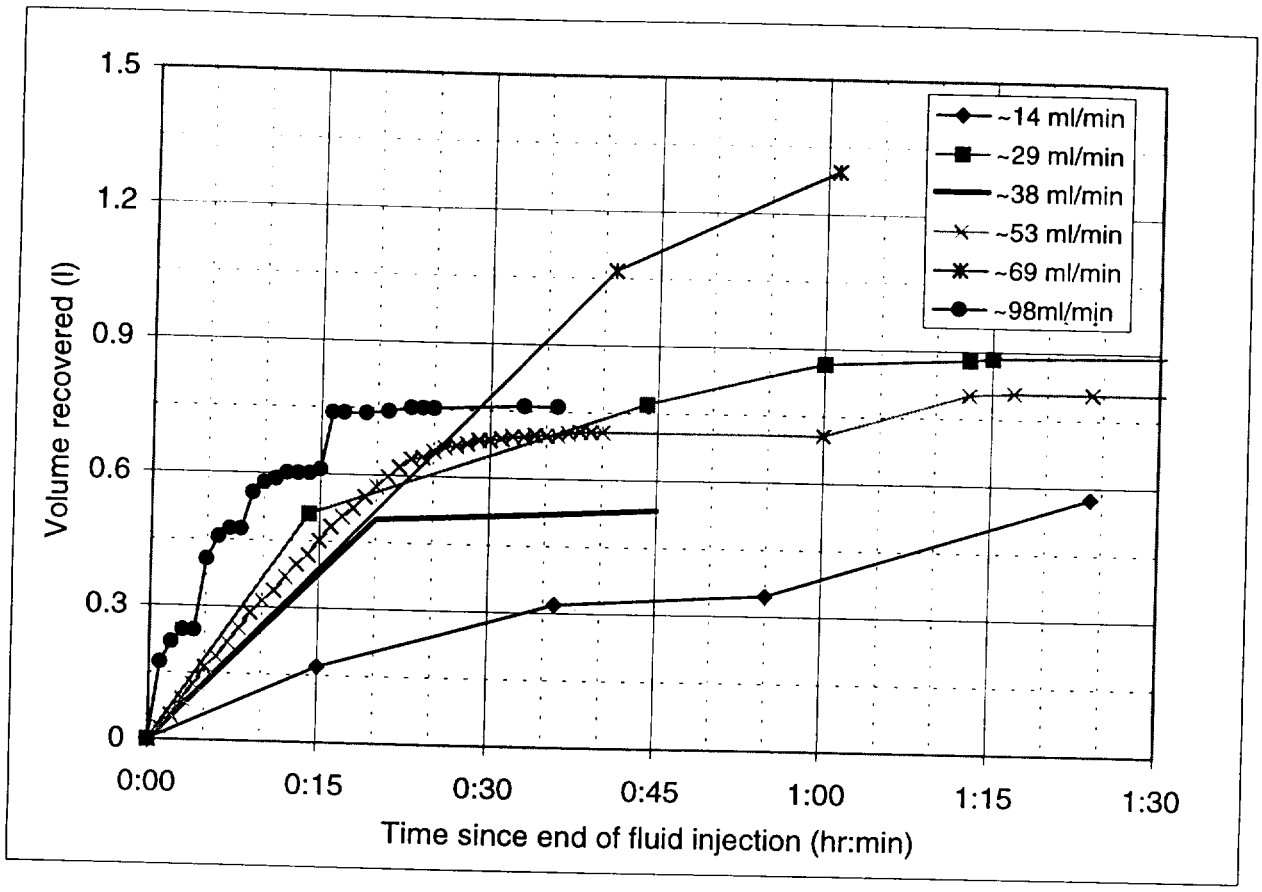

Figure 11. Volume of water recovered in the slot after liquid injection to the HPZ was stopped.

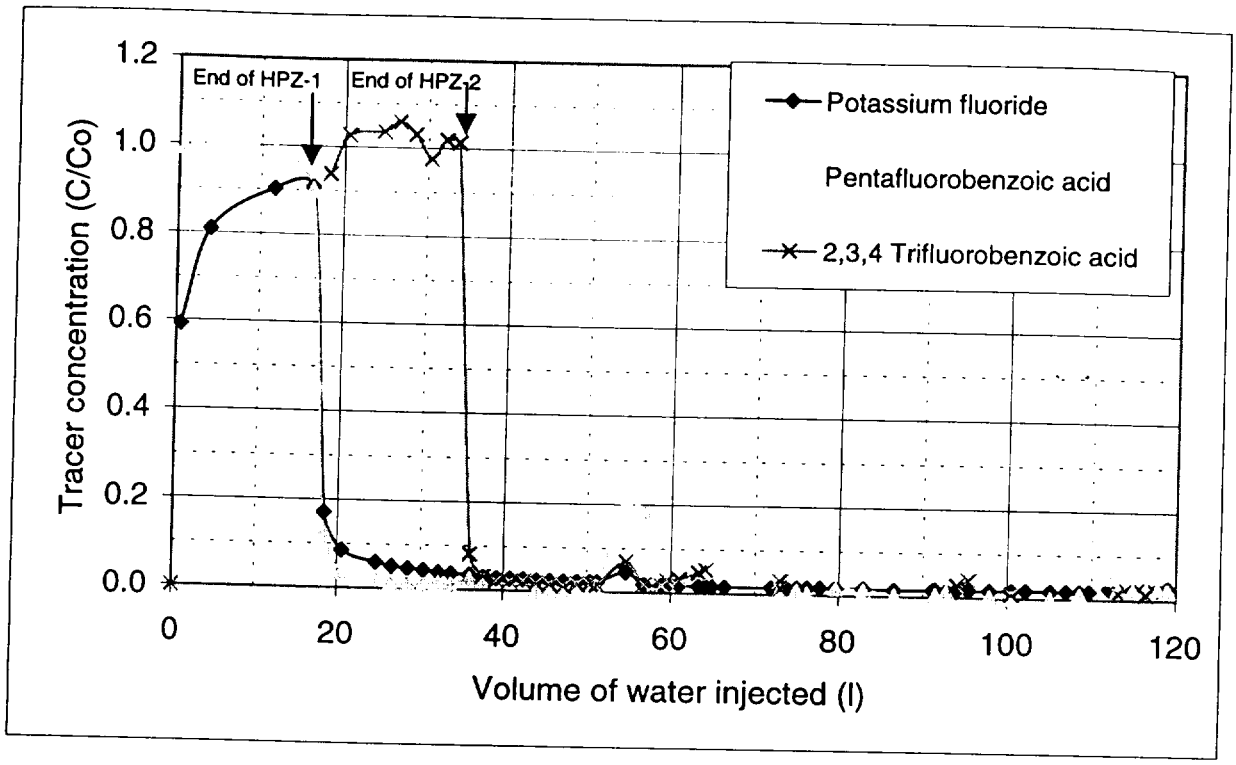

Figure 12. Tracer concentrations in seepage water following injection into the HPZ.

Table 1. Amount of Water and Types of Tracers Released into the Injection Borehole.

Date	Test #	Injection type	Infiltration rate (ml/min)#	Volume of water injected (L)	Additional Tracer *
7/23/98	LPZ-1	Constant rate	~16	5.6	Sodium Bromide 2,3,6 Trifluorobenzoic acid
7/23-24/98	LPZ-1	Falling head			
7/24/98	LPZ-2	Constant head	~1.2	0.3	2,4,5 Trifluorobenzoic acid
7/24-25/98	LPZ-2	Falling head		1.2	2,4,5 Trifluorobenzoic acid
7/29-30/98	LPZ-3	Constant head	~0.5	0.4	3,5 Difluorobenzoic acid
7/30-31/98	LPZ-3	Constant head	~0.5	0.6	3,5 Difluorobenzoic acid
7/31-8/4/98	LPZ-3	Falling head		1.2	3,5 Difluorobenzoic acid
8/4/98 10:23	HPZ-1	Constant head	~119	16.3	Potassium Floride Pentafluorobenzoic acid
8/4/98 17:11	HPZ-2	Constant head	~98	17.3	2,3,4 Trifluorobenzoic acid
8/5/98 9:55	HPZ-3	Constant rate	~53	17.5	3,4 Difluorobenzoic acid
8/6/98 9:08	HPZ-4	Constant rate	~5	3.4	2,3,4,5 Tetrafluorobenzoic acid
8/25/98 8:54	HPZ-5	Constant rate	~69	18.4	
8/26/98 8:25	HPZ-6	Constant rate	~38	18.4	
8/27/98 8:36	HPZ-7	Constant rate	~29	18.2	
8/28/98 8:25	HPZ-8	Constant rate	~14	9.4	

LPZ located 0.75-1.05 m from borehole collar
HPZ located 2.30-2.60 m from borehole collar
Average infiltration rate during release period
* All injected water was tagged with lithium bromide

Table 2. Summary of Liquid Injection Test Results in the High-Permeability Zone

Test #	Injection rate	Duration of injection	Volume injected	Volume recovered	Travel time of first drop	Volume of water in formation		Water retained in formation (%)
						At first drop	At end of injection	
HPZ-1	119	2:17	16.28	11.61	0:05	0.41	4.67	29
HPZ-2	98	2:56	17.44	12.17	0:03	0.17	5.27	30
HPZ-3	53	5:25	17.45	11.14	0:03	0.14	6.31	36
HPZ-4	5	11:54	3.39	0.36	5:00	1.51	3.03	89
HPZ-5	69	4:26	18.37	11.47	0:03	0.14	6.90	38
HPZ-6	38	8:00	18.44	14.73	0:07	0.26	3.71	20
HPZ-7	29	10:36	18.23	13.21	0:07	0.20	5.02	28
HPZ-8	14	11:19	9.38	4.56	1:08	0.90	4.82	51

Volumes in liters
Time in hr:min
Injection rates in ml/min

Liquid Flow in Unsaturated Fractured Welded Tuffs:

II. Numerical Modeling

Christine Doughty, Rohit Salve, and Joseph S.Y. Wang

Earth Sciences Division

Lawrence Berkeley National Laboratory

This work has been supported by the Director, Office of Civilian Radioacitve Waste Management, through Memorandum Purchase Order EA9013MC5X between TRW Environmental Safety Systems, Inc., and the Ernest Orlando Lawrence Berkeley National Laboratory for the Yucca Mountain Site Characterization Project under U.S. Department of Energy Contract No. DE-AC03-76SF00098.

Abstract

We have carried out a numerical modeling study in conjunction with the *in situ* liquid-release experiment described in *Salve et al.* [this issue]. The experiment site is a highly fractured welded tuff accessed from the Exploratory Studies Facility, an underground laboratory in the unsaturated zone at Yucca Mountain, Nevada. The experiment examines the effect of the rock matrix on liquid flow and transport that occurs primarily through the fracture network. The purpose of the modeling is to aid in experimental design, predict experimental results, and study the physical processes accompanying liquid flow through unsaturated fractured welded tuff. The model uses cubic elements arranged in a regular three-dimensional grid to represent a 24 m^3 block of fractured tuff. High-permeability fracture elements located deterministically preserve the connectivity of the fracture network, which is crucial to its ability to conduct fluid. Because element thickness is much greater than fracture aperture, fracture elements are assigned properties of a fracture continuum rather than of an individual fracture. The fracture network is constructed using fracture geometry data taken from a fracture map of the walls and ceiling of the alcove adjacent to the field test site. The network is then refined using the results of air-permeability tests. Model results suggest that it may not be sufficient to conceptualize the fractured tuff as consisting of high-permeability fractures embedded in a low-permeability matrix. The need to include a secondary fracture network (with distinct characteristics from the network of larger mapped fractures) is demonstrated by comparison to the liquid flow observed in the field.

1. Introduction

In this paper, we investigate the manner in which subsurface liquid flow is distributed between the fracture network and the surrounding rock matrix in an unsaturated, highly fractured welded tuff known as the Topopah Spring welded unit (TSw). The TSw is the host rock for a potential nuclear waste repository at Yucca Mountain, Nevada. Field experiments have been recently conducted in the Exploratory Studies Facility (ESF), an underground laboratory in the unsaturated zone at Yucca Mountain. The background and motivation for the fieldwork known as the fracture-matrix interaction test, as well as a detailed description of its procedures and results, are described in a companion paper [*Salve et al.*, this issue]. The present paper is concerned with numerical modeling studies conducted in conjunction with the test. Below, we briefly outline the features of the test that the model attempts to reproduce and describe the motivation for the modeling studies. In Section 2, conceptual and numerical models are described, followed by model results in Sections 3 and 4, and some concluding remarks in Section 5.

The fracture-matrix interaction test site is a rock block located in the right wall (rib) of Alcove 6 in the ESF [See *Salve et al.*, this issue, Figure 1]. It includes several horizontal boreholes drilled into the alcove wall overlying an excavated slot. Under ambient (pre-test) conditions, there is no seepage into the slot, and liquid percolation through the partially saturated system is assumed to be small. Water is released into a packed-off interval in one borehole, moisture changes are monitored in the other boreholes, and water seeping into the slot is collected. The configuration of the boreholes and slot is designed so that the slot can capture essentially all released water not imbibed by the

matrix or trapped within the fracture network. In a series of tests, water is released into two zones, one with low permeability and the other with relatively high permeability, using a variety of flow rates. The times and location of water arrivals at the slot ceiling, as well as volume balances of water released into the borehole and collected at the slot, are used to investigate fracture-network geometry and matrix imbibition.

The present modeling studies have two primary objectives. The first is to aid in the experimental design of the fracture-matrix interaction test. Numerical modeling is used to study which physical processes are important and the sensitivity of these processes to model parameters under various experimental conditions, thereby helping to determine the optimal way to run the experiments. Experimental conditions that are investigated include liquid-release rate and test duration. Fracture properties such as network connectivity, permeability, porosity, and capillary pressure strength control the gross features of the test, such as the volume of water that can be injected and the time required for the water to arrive at the slot. The effect of these properties must be understood before we can infer fracture-matrix interaction effects from the experimental results.

The second objective is to model the experiments and compare the modeled and observed results, to assess our state of understanding, interpret the observed results, and recognize the capabilities and shortcomings of the models. Examining the similarities and discrepancies between model and test results leads to better understanding and improvement of conceptual models, numerical techniques, and field test designs,

ultimately resulting in better quantification of fracture flow, fracture-matrix interaction, and matrix imbibition.

2. Methodology

2.1. Conceptual Model for Fracture Network

The modeling approach assumes that the multi-phase extension of Darcy's law governs fluid flow in both fractures and rock matrix. Spatial discretization is fine enough to represent individual fractures and their intersections deterministically, as illustrated in Figure 1. Space is discretized into cubic gridblocks, or elements, and fractures are modeled as disks with a one-element thickness. The elements composing the fracture disks are denoted fracture elements. They are assigned properties of a fracture continuum rather than properties of an individual fracture, to account for actual fracture aperture ($\sim 10^{-4}$ m) being much less than element thickness (0.15 m). Intersections between two fracture disks are line segments, and the fracture elements representing intersections can be assigned special properties if desired. Any element that is not part of a fracture disk is denoted a matrix element and is assigned properties of the intact rock matrix. Fracture-matrix interactions (i.e., imbibition, drainage, chemical diffusion) potentially occur wherever fracture elements are connected to matrix elements. Note from Figure 1a that no special grid refinement exists at such locations. The coarse grid spacing makes this fracture-matrix treatment comparable to the quasi-steady dual porosity approach of *Barenblatt et al.* [1960] and *Warren and Root* [1963].

The present modeling approach is considered a quasi-explicit fracture-network representation, in that the fractures are individually resolved, but not modeled using element dimensions commensurate with actual fracture apertures. It is far more straightforward to implement and less computationally intensive than would be a truly explicit fracture-network representation [e.g., *Therrien and Sudicky*, 1996]. Thus, it is more appropriate for the present work, which involves iteratively modifying the model as additional data becomes available.

The quasi-explicit fracture-network approach is of comparable resolution and detail to the stochastic models recently used for numerical modeling of similar scale problems at Yucca Mountain [e.g., *Birkholzer et al.*, 1999; *Birkholzer and Tsang*, 1997] in that submeter-sized elements arranged in a regular grid are used to represent both fractures and rock matrix blocks as continua. However, the present work has a fundamentally different underlying premise, in which high-permeability fracture elements are located deterministically rather than stochastically. The scale of the fracture-matrix interaction test (a few meters) is not much larger than the 0.53 m fracture spacing calculated for the lithostratigraphic zone in which the test site is located [*Sonnenthal et al.*, 1997]. Hence, the vertical and lateral connectivity of the fracture network at the test site can be represented much more realistically with a deterministic model than with a stochastic model that considers the permeability distribution to be a realization of a correlated random field, constructed using variograms based on fracture trace measurements collected over a large area. The capability to represent actual individual fractures is

important at the present scale, where an understanding of fracture-network geometry is crucial for interpreting test results and thereby inferring fracture-matrix interactions.

For liquid flow studies at very large scales, such as the consideration of percolation from the ground surface to the potential repository level hundreds of meters below, depicting every fracture explicitly (or even quasi-explicitly) is not practical, but dual continuum models enable fracture-matrix interactions to be incorporated without representing individual fractures [*Doughty*, 1999a; *Wu et al.*, 1999; *McLaren et al.*, 2000]. Comparing various percolation and seepage tests conducted at the smaller scales involved in recent ESF experiments (niche seepage studies, an infiltration test in Alcove 1, and the fracture-matrix interaction test [*Wang et al.*, 1998]) illustrates the need for a different type of model for each scale. For the niche seepage studies, water was released into packed-off intervals in a horizontal borehole less than one meter above an excavated niche, and seepage through the niche ceiling was monitored. Since typical fracture spacing is on the order of one meter, flow was expected to occur through a single fracture or a few discrete fractures. Field observations support this notion, with dye generally observed along a fracture trace just below the point at which it was released [*Wang et al.*, 1999]. These tests considered liquid releases of short duration under ponded or high release rate conditions that minimize the impact of the rock matrix. Mineback after the tests confirmed that flow paths followed fractures and matrix imbibition effects were minimal. Hence, a fracture-only model is appropriate. For the Alcove 1 infiltration test, the test scale is about 30 m, the distance from an infiltration pond at the ground surface to the alcove ceiling. This test site is too large to allow individual fractures to be modeled

explicitly. Fracture data are only available at the upper and lower surfaces of the test site, and the distance between these surfaces is too great to allow extrapolation of fracture geometry with any confidence. Conversely, the distance is large enough that the effects of individual fractures tend to average out, making a dual continuum model appropriate for this test. At the scale of the fracture-matrix interaction test, a few meters, neither of the above approaches is well justified. Thus, a deterministic model of the fracture network and surrounding rock matrix is the most reasonable conceptual alternative, and the quasi-explicit fracture network is the most computationally tractable means of representing it numerically.

A similar quasi-explicit fracture-network representation was used to model a ponded infiltration test in the Snake River basalt in southeastern Idaho, where the fractures form a highly structured columnar joint pattern [*Doughty*, 1999b, 2000]. The field site was about 20 m wide, with the primary vertical fractures separated by about 5 m, nearly the same ratio as at the fracture-matrix interaction test site (a 2 m wide test site and 0.53 m fracture spacing). Field observations were compared with results of the quasi-explicit fracture-network model and a traditional stochastic model constructed using variograms, which did not necessarily preserve fracture connectivity. The comparisons indicated that representing the actual fracture-network geometry provided much greater insight into flow and transport processes.

The primary data used to construct the fracture-network model of the fracture-matrix interaction test site are the fracture strikes, dips, and locations obtained from the Alcove 6

fracture map (Figure 2). Air-permeability measurements [*Salve et al.*, 1998] made along the three boreholes overlying the slot are then checked for consistency with projected fracture locations, and strikes and dips are modified as necessary. Initial conditions and material properties are mainly taken from an unsaturated zone model encompassing all of Yucca Mountain (the UZ site-scale model; *Ritcey et al.* [1998]), with some fracture properties derived from smaller-scale studies conducted at the ESF [*Sonnenthal et al.*, 1997; *Freifeld and Tsang*, 1998]. Other data that can potentially be used in model development include core logs and photos, borehole video and scanner images, geophysical logs, and results of liquid-release tests.

2.2. Limitations of Conceptual Model

Several important limitations to the present fracture-network model are enumerated below, along with suggested remedies.

First, there is little corroboration of fracture geometry from beyond the plane of the alcove wall. That is, there is minimal 3-D control on the fracture locations and orientations mapped at the wall. Hence, the extent of fractures into the rock is unknown, as are departures from planar geometry. Correlating fracture traces mapped at the alcove wall with fractures observed in boreholes would remedy this limitation. Mapping fractures that appear in boreholes, but are not seen at the alcove wall, would also provide additional information. Useful existing data include core, core photos, and borehole video. Other types of data that might prove useful include borehole scanner imaging and slot-ceiling imaging.

Second, even with complete information on the geometry of all the fractures that exist in the test block, the model would not necessarily predict hydrologic behavior correctly. Fracture geometry alone does not predict whether or not the fracture network is conductive. We can use observations on fracture aperture, asperities, and infilling material to begin to estimate fracture conductivity, but in general these small-scale measurements cannot be extrapolated to the field scale because fractures are very heterogeneous. The most reliable way to determine fracture-network conductivity is to run field-scale tests of the connectivity of the fracture network, such as crosshole air-permeability tests or liquid-release tests. In other words, we can best construct a model in an inverse mode, using the very data we want to predict to determine the model parameters.

Third, the adequacy of the quasi-steady approximation for fracture-matrix flow has been examined in detail for the UZ site-scale model of Yucca Mountain [*Doughty*, 1999a], where it was found to work well under some conditions and not so well under others. In general, the quasi-steady approach may underestimate fracture-matrix flow under transient conditions, because it does not include the fine matrix resolution adjacent to fracture-matrix interfaces that is necessary to represent the steep pressure and concentration gradients that may develop during transient fracture-matrix interactions. Preliminary scoping studies (Section 3.3) conducted at the scale of the fracture-matrix interaction test suggest that this underestimation can happen for the quasi-explicit

fracture-network representation as well. This fact must be kept in mind when evaluating the present results.

Finally, in the present fracture-network model, each fracture can have different flow properties (permeability, porosity, and characteristic curves), but heterogeneity within individual fractures is not explicitly taken into account. There is, however no fundamental reason why this approximation could not be alleviated. Fracture element property distributions could be constructed as random fields or assigned deterministically if sufficient characterization had been done.

2.3. Numerical Model Development

We have written a simple mesh generator called FRACGRID to implement the quasi-explicit fracture network concept described above into a numerical model. FRACGRID output is in the specific form required by TOUGH2, the flow and transport code used to simulate the liquid-release tests. Below, we briefly describe TOUGH2 and then illustrate how FRACGRID is used to create a model of the fracture-matrix interaction test bed.

The TOUGH2 Numerical Simulator

TOUGH2 [*Pruess*, 1987, 1991] is a general-purpose code that simulates two-phase flow of air and water in gaseous and liquid phases together with tracer and heat transport through porous or fractured geologic media (which may be strongly heterogeneous). Darcy's law governs fluid flow through both the fractures and rock matrix, with relative

permeability and capillary pressure specified as functions of liquid saturation to describe the flow and transport between liquid and gas phases. Relative permeability and capillary pressure functions were developed to describe multi-phase flow in porous media [*Scheidegger*, 1974], but in the past decade they have been widely applied to fractured rock [e.g., *Pruess and Tsang*, 1990; *Reitsma and Kueper*, 1994; *Persoff and Pruess*, 1995 and references therein]. TOUGH2 offers a variety of equation of state (EOS) modules to customize the code to the problem at hand. The EOS module used for the present studies [*Wu et al.*, 1996] considers only liquid-phase flow under isothermal conditions, with the gas phase considered to be a passive spectator (Richards' equation). TOUGH2 uses the integral finite difference method (IFDM) for spatial discretization [*Edwards*, 1972; *Narasimhan and Witherspoon*, 1976], which offers greatly increased flexibility in grid design compared to typical finite difference methods. For a regular lattice of cubic gridblocks as used here, the IFDM is equivalent to a block-centered finite difference scheme.

TOUGH2 is widely used in the research community and consulting industry for a variety of problems, including environmental remediation, geothermal and petroleum reservoir engineering, and nuclear waste isolation [*Pruess*, 1995, 1998]. Its ability to model two-phase flow in fractured rock is supported by verification with analytical solutions, comparison to laboratory and field data, benchmarking against other codes, and systematic studies of numerical behavior [*Pruess*, 1987, 1991; *Pruess et al.*, 1990a,b; *Moridis and Pruess*, 1992, 1995; *Doughty*, 1999a]. Of particular relevance for the present problem are verification with a semi-analytical solution for one-dimensional

infiltration [*Philip*, 1955; *Pruess*, 1987], validation to a two-dimensional laboratory infiltration experiment [*Vauclin et al.*, 1979; *Moridis and Pruess*, 1992], and comparisons of conceptual and numerical approaches for modeling flow and transport in unsaturated fractured rock [*Pruess et al.*, 1990a,b; *Doughty*, 1999a].

The FRACGRID Mesh Generator

As described in Section 2.1, we want to locate individual fractures deterministically, but represent the fractures with regular-size elements having fracture-continuum properties. We conceptualize individual fractures as planar disks identified by strike, dip, a reference coordinate (e.g., a point along the fracture trace on the alcove wall), a center point, and a radial extent, from which we can determine the equation and extent of the fracture plane in (x,y,z) coordinates. The model domain is then discretized into a 3-D regular Cartesian grid, and it is straightforward to determine which gridblocks each fracture disk passes through. These elements are then assigned a material type representative of the fracture continuum. Elements through which multiple fracture disks pass are assigned a special material type to represent fracture intersections. Elements through which no fracture disks pass are assigned a material type representative of the matrix continuum. If desired, these matrix elements may be omitted, leaving a model consisting only of the fracture network.

With both fracture and matrix elements included, treatment of fracture-matrix interactions is similar to that of a dual permeability model in which one matrix element is associated with each fracture element. This approach enables a quasi-steady treatment of

fracture-matrix flow. With no matrix elements included, we may investigate just the response of the fracture network.

Figure 2 shows a portion of the Alcove 6 as-built geology and geotechnical data [*Beason*, 1997], and Table 1 lists the 17 fractures in the vicinity of the fracture-matrix interaction test site that are used as input for the FRACGRID mesh generator. Strike and dip values are read off Figure 2, and reference coordinates are determined by projecting fracture traces to the horizontal line shown at a height of about 1 meter above the base of the right wall. Fracture radii are assumed infinite for most of the fractures, which makes the fracture center point irrelevant. For several fractures that show short traces on the alcove wall, shorter radii are used, and fracture center points near the alcove wall are assumed. These assumptions of fracture radii and center points are the most uncertain aspect of the model geometry and would greatly benefit from borehole fracture information.

The model coordinate system uses x as the distance along the alcove wall (increasing from the entrance to Alcove 6, the coordinate system used for fracture mapping), y as the distance perpendicular to the alcove wall ($y = 0$ at the wall, with negative y values in the rock), and z as the vertical distance ($z = 0$ at the alcove floor, increasing upward).

Figure 3 shows the preliminary 3-D model constructed using the parameters given in Table 1. The grid spacing is 0.15 m. Intersections between two or more fractures are not shown explicitly, enabling the fracture pattern to be visualized more easily in densely fractured regions. The cut-away view shows a cross section through the model aligned

with injection borehole A, which is located about 1.6 m above the top of the 2 m wide slot. Figure 4 shows air-permeability measurements taken along injection borehole A and observation boreholes C and D, which are located about 0.6 m below and 0.35 m to either side of borehole A [*Salve et al.*, this issue, Figure 1]. The high permeabilities shown between $y = -2$ and -2.5 m in the injection borehole coincide with visual identification of a large fracture, and this interval, denoted the high-permeability zone (HPZ), is one of the liquid-release locations. The model does not show a fracture at this location (see Figure 3), but does show a likely candidate, Fracture 10, that intersects the injection borehole at $y = -1$ m. We conjecture that Fracture 10 is the fracture observed in the injection borehole, increase its strike from 124 to 152 degrees in the FRACGRID input, and recreate the 3-D model. With this change, Fracture 10 intersects the injection borehole at about $y = -2$ m, as shown in Figure 5.

Although it is certainly possible that the fracture identified visually in the injection borehole at the HPZ is not the same Fracture 10 mapped on the alcove wall, we consider it plausible that it is. Fracture 10 is a vertical fracture, and water released at the HPZ was observed in the slot nearly directly below the release point. The character of the air-permeability profile for the injection borehole suggests a few localized fractures separated by intact rock, which agrees with the 3-D model. Strikes measured at the alcove wall are often based on very limited observations, and may not represent the large-scale average strike of a fracture. Figure 5 indicates that Fracture 10 also intersects observation boreholes C and D, and the air-permeability profiles in these boreholes (Figure 4) show medium to high permeability values at those locations. One way to test

the 3-D model would be to run interference air-permeability tests between these intervals and look for evidence of high conductivity between them.

Other minor discrepancies exist between the air-permeability profiles and the 3-D model (e.g., Fractures 3 and 4 appear to intersect the injection borehole too close to the alcove wall in the model). These discrepancies were not addressed for the present study because they are not associated with liquid-release locations. In addition to the HPZ about 2 m from the alcove wall, water was released into a low-permeability zone (LPZ) about 1 m from the alcove wall, where the model shows no fractures.

Even without flow simulations, the construction and visualization of the 3-D model is a useful exercise, enabling insights into fracture geometry and thereby greatly aiding interpretation of experimental results. For example, the oscillating water potential observed in borehole D at $y = -1.9$ m [*Salve et al.*, this issue, Figure 8d] suggests strong communication with atmospheric pressure variations in Alcove 6. Creating a cut-away view of the model similar to Figure 5, but along observation borehole D, shows that Fracture 16 provides a potential pathway from the sensor location to the Alcove 6 wall.

3. Results of Preliminary Scoping Studies

The primary results of the fracture-matrix interaction test that the model attempts to match are the time, t_{bt}, and location at which injected water breaks through into the slot (breakthrough is denoted by the subscript *bt*); the cumulative fraction of injected water

that is recovered at the slot, M_{slot}/M_{inj}, as a function of time; and temporal variations of capillary pressure measurements made in the two observation boreholes overlying the slot [*Salve et al.*, this issue]. Before applying the 3-D fracture-network model to this problem directly, we examine several simpler analytical and numerical models to gain insight into the physical processes taking place during liquid-release tests in fractured tuff.

3.1. 1-D Analytical Solution for Gravity-Driven Flow

If we consider purely gravity-driven liquid flow in a vertical fracture that is originally near residual saturation, we can predict t_{bt} with an analytical expression. This value of t_{bt} provides a lower bound on expected field behavior, because capillarity within the fracture plane and fracture-matrix interactions act to lengthen t_{bt}. It is applicable for single liquid-release tests or the first of a series of tests, but may overpredict t_{bt} for a test conducted soon after a previous test, before liquid saturations have returned to ambient levels.

Consider an injection interval located a distance Δz above a slot, with injection at a volumetric rate q_{inj} into a uniform fractured continuum of permeability k_f, porosity ϕ_f, and relative permeability k_{rlf}. We approximate the area through which gravity flow occurs as $A = \pi rL$, where r is the borehole radius and L is the injection interval length. If q_{inj}/A is greater than fracture hydraulic conductivity, then ponded conditions occur, with fracture saturation S_{lf} becoming one. For negligibly small ponding height, Darcy's law with a unit head gradient equates flow rate per unit area q/A to fracture hydraulic conductivity:

$$\frac{q}{A} = \frac{k_f \rho g}{\mu} \tag{1}$$

where μ and ρ are the viscosity and density of water, respectively, and g is gravitational acceleration. On the other hand, if $q_{inj}/A < k_f\rho g/\mu$, then $S_{lf} < 1$ and flow rate per unit area is simply

$$\frac{q}{A} = \frac{q_{inj}}{A}. \tag{2}$$

Combining these expressions yields

$$\frac{q}{A} = \min\left(\frac{q_{inj}}{A}, \frac{k_f \rho g}{\mu}\right). \tag{3}$$

Darcy velocity q/A can be converted to average pore velocity v_p by dividing by ϕ_f and S_{lf}:

$$v_p = \frac{\min(q_{inj}/A, k_f \rho g/\mu)}{\phi_f S_{lf}}. \tag{4}$$

Noting that $t_{bt} = \Delta z/v_p$ yields

$$t_{bt} = \frac{\Delta z \phi_f S_{lf}}{\min(q_{inj}/A, k_f \rho g/\mu)}. \tag{5}$$

Thus, under slightly ponded conditions, $S_{lf} = 1$ and t_{bt} depends directly on ϕ_f and inversely on k_f. When the injection rate is too low to cause ponding, the expression looks simple, but there are dependencies on k_f, q_{inj}/A, and the functional form of $k_{rlf}(S_{lf})$ implicit in the value of S_{lf}, which is obtained from Darcy's law under unsaturated conditions

$$\frac{q}{A} = \frac{q_{inj}}{A} = \frac{k_f k_{rlf}(S_{lf})\rho g}{\mu} \tag{6}$$

for a given functional form $k_{rlf}(S_{lf})$ (e.g., a *van Genuchten* [1980] expression). Note that for a linear relative permeability function ($k_{rlf}(S_{lf}) = S_{lf}$), the saturation dependence drops out of Equation (5) and the partially-saturated and fully-saturated expressions for t_{bt} become identical. For most realistic relative permeability functions, $k_{rlf}(S_{lf}) << S_{lf}$ and t_{bt} grows as S_{lf} decreases in response to a decrease in q_{inj}.

Using Equation (5) to model the results of niche seepage tests at the ESF [*Wang et al.*, 1999] suggests that fracture porosity ϕ_f is in the range 2– 4% [*Salve et al.*, 1998], significantly larger than the fracture porosity value of 10^{-4} used for the UZ site-scale model. An increase in apparent ϕ_f is expected when a relatively small rock volume centered on a specific fracture (as in the niche seepage tests) is compared to a large rock volume containing many fractures (as in the site-scale model). However, consideration of typical fracture spacing and injection interval dimensions shows that the increase in ϕ_f expected on geometric grounds is less than a factor of five. Use of a large ϕ_f is supported

by numerical modeling studies of the niche liquid-release tests that were conducted using "drift-scale parameters", including $\phi_f = 0.1\%$ [*Wang et al.*, 1999]. A relatively large fracture porosity value ($\phi_f \approx 0.5\%$) was also obtained from analysis of gas-phase tracer tests conducted as part of the drift-scale heater tests at the ESF [*Freifeld and Tsang*, 1998].

Table 2 shows the value of t_{bt} obtained from Equation (5) over a range of q_{inj} values, for conditions considered plausible at the fracture-matrix interaction test site. A *van Genuchten* [1980] relative permeability function with $m = 0.63$ and $S_{lr} = 0.01$ is used, along with $\phi_f = 0.01$, $A = 0.05$ m^2, $\Delta z = 1.6$ m, and $\mu/\rho g = 10^{-7}$ m·sec. Recall that Equation (5) does not consider capillary spreading within the fracture or fracture-matrix flow, processes that will have greater relative importance for longer breakthrough times. Hence, while all the values of t_{bt} shown in Table 2 merely provide lower limits for expected field behavior, the larger values are more likely to be significantly too low. In contrast, for closely spaced tests, history effects not included in the analytical solution could shorten breakthrough times compared to those shown in Table 2.

3.2. 2-D Numerical Model of a Single Fracture

TOUGH2 is used with a 2-D model of a single vertical fracture intersecting a slot to examine the interplay of gravity and capillary forces during a liquid-release test, to verify the 1-D gravity-only analytical solution for t_{bt}, and to examine the effect of the slot. The model represents a homogeneous planar fracture, 4 m high and 7 m wide. An injection borehole intersects the fracture about 2 m above the top of a 5 m wide slot, which makes

up most of the bottom boundary of the model (with the fracture extending 1 m on either side). The top and side boundaries of the model are closed, and the bottom boundary allows liquid to flow out freely. A series of simulations considers a range of constant injection rates q_{inj}, fracture permeabilities k_f, and van Genuchten α parameter, which is inversely proportional to capillary pressure strength. Prior to simulating a liquid-release test, we establish natural-state conditions by imposing a percolation rate of 7 mm/yr at the top of the model and letting the model run to steady state. The test is then modeled by injecting water into the borehole at a constant rate. The key performance measures are the breakthrough time at the slot t_{bt} and the width of the injected-liquid plume at the slot after a long period of injection. Plume width is defined as the width of the zone through which 95% of the liquid flow occurs.

Breakthrough time is found to depend strongly on k_f and q_{inj}, in agreement with the analytical solution, and weakly on α_f. For capillary pressure $P_{cap} = 0$ (reasonably approximated by $\alpha_f = 0.1$ Pa^{-1}), the numerical model matches the analytical solution given by Equation (5) well. As α_f is decreased, t_{bt} grows slowly. In contrast, the width of the plume, both at the slot and throughout the fracture, depends strongly on α_f, with smaller values of α_f yielding a wider plume. The maximum liquid saturation in the plume does not depend strongly on α_f, but rather on the combination of k_f and q_{inj}.

Under ambient conditions (a percolation rate of 7 mm/yr), the slot acts as a capillary barrier, with liquid saturation increasing above it and natural-state percolation flowing around rather than into it. For all the constant-rate liquid-release tests simulated, the flow

is strong enough to overcome the capillary barrier and water flows into the slot. In contrast, for a pulse test at a low injection rate in which liquid release is halted before breakthrough at the slot, water does not enter the slot, but is diverted around it. For a pulse test at a moderate injection rate, breakthrough occurs at the slot much later than for a constant-rate test. Modeling a sequence of liquid-release tests with short rests between them shortens breakthrough time significantly for the later tests.

Modeling the slot with a relative humidity less than one does not affect breakthrough time, but does narrow the width of the plume at the slot. Modeling the slot as a water-saturated boundary prior to a liquid-release test, to simulate the effects of the wet excavation technique used for the slot, does not change t_{bt} either.

Results of the single-fracture model lend credence to the use of the analytical solution as a first approximation for predicting t_{bt}, which is needed to determine the overall schedule of the field test. The analytical solution is expected to provide reasonably good estimates (1) when breakthrough occurs in a narrow zone, suggesting that α_f is large (capillary strength is weak); (2) when tests are separated widely enough in time to allow natural-state conditions to be re-established before each test; and (3) when breakthrough time is short, precluding fracture-matrix interactions from playing a significant role. The single-fracture model may be used when either of the first two conditions is not met. The model described in Section 3.3 enables consideration of fracture-matrix interactions.

3.3. 2-D Numerical Model of a Single Fracture with Matrix

The single-fracture model described above is modified by adding elements to represent the surrounding rock matrix. Fracture permeabilities and all matrix properties are taken from the UZ site-scale model and are based on calibration to natural-state field observations. Fracture porosity is based on the niche seepage studies described in conjunction with the analytical solution. The fracture characteristic curve parameters (van Genuchten α_f and m_f) are inferred from fracture data collected in the ESF [*Sonnenthal et al.*, 1997]. The fracture initial liquid saturation is adjusted to produce a natural-state percolation rate of about 7 mm/year. All the parameters used in the single fracture with matrix model are summarized in Table 3.

In general, rock matrix adjacent to a fracture should be finely discretized in the direction perpendicular to the fracture plane to rigorously calculate transient fracture-matrix flow [*Pruess*, 1991; *Doughty*, 1999a]. We conduct TOUGH2 simulations using different matrix discretizations to investigate the calculation of transient fracture-matrix flow under the conditions of the present liquid-release tests. Dividing the rock matrix into three, four, or five elements per fracture element produces similar results, implying that three is sufficient. Using one matrix element per fracture element, as is done in the quasi-explicit fracture-network model, tends to underestimate fracture-matrix flow before t_{bt} (i.e., when regions of newly wet fracture are initiating matrix imbibition) and overestimate it thereafter (since the overall imbibition capacity of the matrix does not depend on how the matrix is discretized, the early-time imbibition deficit must be offset) . In contrast, breakthrough time at the slot is not very sensitive to the number of matrix

elements used. Thus, we expect that use of the quasi-explicit fracture-network model will be adequate for studying t_{bt}, but may not be reliable for making quantitative predictions about matrix imbibition.

The single fracture with matrix model is used to address two experimental design issues for the liquid-release tests: the choice of injection rate and the duration of the injection period. We want to choose these parameters to facilitate determination of the fractions of injected water recovered at the slot and imbibed into the matrix, as well at breakthrough time t_{bt}. Because the matrix imbibition rate cannot be measured in the field, we must try to infer it from the injection rate and the slot seepage rate.

To assess the impact of injection rate on matrix imbibition, we note that the rock matrix is quite wet under ambient conditions (Table 3). Thus, the fraction of injected water that is imbibed into the matrix is expected to be small and we want to design the liquid-release tests so as to maximize it. The more slowly liquid moves downward through the fracture network under the force of gravity, the more time will be available for matrix imbibition. According to Equation (5), t_{bt} (and more generally, the residence time in the fracture network between the injection interval and the slot) is maximized by minimizing q_{inj}. Hence, to optimize the study of matrix imbibition, we should use the lowest injection rate practical. TOUGH2 simulations using different injection rates confirm this notion. At a low injection rate (6 ml/min), shortly after t_{bt} at 72 minutes about 12% of the injected water has been imbibed into the matrix, whereas at a high injection rate (60 ml/min), t_{bt} is 10 minutes and the cumulative imbibition is less than 5%.

The value of using low injection rates for studying matrix imbibition must be balanced by logistical requirements that may favor high injection rates in order to produce shorter breakthrough times and thereby allow experiments to be completed within manageable time frames. An alternative means of increasing matrix imbibition is to use a location with low initial matrix saturation. For example, a TOUGH2 simulation with an initial matrix saturation of 0.6 yields 36% imbibition for the low injection rate, along with a t_{bt} of 86 minutes.

The second experimental design issue is the duration of the injection period. Based on studies with the single fracture model described in Section 3.2, the duration of the injection period should always be greater than t_{bt}, in order that values of t_{bt} for different injection rates can be compared in a straightforward manner. Figure 6 shows results for a TOUGH2 fracture with matrix simulation that illustrates how long the injection period need be to infer the relative matrix imbibition rate (q_{imb}/q_{inj}) from measurements of the cumulative fraction of injected water recovered at the slot (M_{slot}/M_{inj}). Differentiating M_{slot} with respect to time and normalizing by q_{inj} yields the fractional slot seepage rate (q_{slot}/q_{inj}). In theory, q_{slot} could be taken from values measured directly in the field, but as shown in *Salve et al* [this issue, Figure 9] q_{slot} may be too highly variable to use directly. Shortly after t_{bt}, q_{slot}/q_{inj} and M_{slot}/M_{inj} are small but rapidly increasing, reflecting transient flow through the fracture. At later times, both begin to level off, q_{slot}/q_{inj} when quasi-steady flow conditions are established in the fracture, and M_{slot}/M_{inj} when the volume of water injected is large compared to the volume injected at t_{bt}. Shortly after q_{slot}/q_{inj} levels

off, the fractional flow rate not recovered at the slot, $(1- q_{slot}/q_{inj})$, becomes a reasonable approximation for the fractional imbibition rate q_{imb}/q_{inj}. A series of TOUGH2 simulations using different injection rates indicates that for the parameters given in Table 3, this condition develops at times equal to about $15 \cdot t_{bt}$.

An analytical solution for matrix imbibition predicts that imbibition rate q_{imb} has a $t^{-1/2}$ time-dependence [*Zimmerman and Bodvarsson*, 1989]. This is consistent with the time depencences shown in Figure 6, where the late-time portions of q_{slot}/q_{inj} and M_{slot}/M_{inj} are gradually increasing and q_{imb}/q_{inj} is gradually decreasing. Thus, if the duration of the injection period is very long and M_{slot}/M_{inj} is just measured once at the end, nearly all of the injected water will have appeared at the slot (i.e., $M_{slot}/M_{inj} \approx 1$), providing little or no information about imbibition. Therefore, we should begin measuring M_{slot}/M_{inj} as soon after t_{bt} as possible and look at its entire time variation, not just the final value.

4. Results of the 3-D Quasi-Explicit Fracture-Network Model

TOUGH2 simulations of the liquid-release tests conducted in the LPZ and HPZ use the 3-D model of the fracture-matrix interaction test site shown in Figure 5. The 0.3 m long packed-off intervals of the injection borehole are each modeled by two adjacent 0.15 m wide gridblocks. For the LPZ tests, the injection gridblocks are surrounded by matrix gridblocks and flow out of the borehole is expected to be slow, so it is important to include the effect of the injection interval itself. The permeability of the injection gridblocks is set to a large value, and porosity is set to 0.25, so that pore volume

approximates the borehole volume that can fill with water (i.e., the portion of the cylindrical borehole below the return flow line; see *Salve et al.*, this issue, Figure 2b). The surface area of the injection gridblocks is also modified to match that of the injection interval. For the HPZ tests, the injection gridblocks are located where Fracture 10 intersects the borehole (Figure 5) and flow out of the borehole is expected to be fast. Hence, the material properties of the injection gridblocks are the same as those of the fracture.

Table 1 of *Salve et al.* [this issue] shows the time schedule and liquid-release rates used for the tests. Some of the tests were conducted as constant-head or falling-head tests, but they are all modeled as prescribed flow-rate tests, using averages of observed flow rates. A key requirement for developing a realistic model is to release the right amount of water into the formation, and this can be achieved more easily with a prescribed flow-rate boundary condition than with a prescribed head boundary condition.

4.1. LPZ Tests

Original Model

We first attempt to model test LPZ-1 using the same material properties as for the 2-D simulations described in Section 3.3. These properties are given in Table 3 and include matrix properties from the UZ site-scale model. For initial saturation conditions in the matrix, we consider two cases. In the first, we use the usual site-scale model value (0.928), which corresponds to a capillary pressure of about –40 m and is considered to

represent natural-state conditions. For the second, we use a lower value (0.75) that corresponds to a capillary pressure of about −150 m. Such capillary pressures have been observed near alcove and niche walls [*Salve et al., 1997; Salve and Wang*, 1998] as drying fronts propagate into the rock from the drift wall as a result of ventilation (Figure 7).

Model results show that neither case can maintain the specified LPZ-1 injection rate unless a huge pressure increase occurs around the injection interval. This is not surprising when we consider that an injection rate of 0.35 ml/min (the final value observed during the LPZ tests [*Salve et al.*, this issue, Figure 5a]) distributed over an area of about 0.1 m^2 (the surface area of the injection interval below the return flow line) corresponds to a Darcy velocity of about $5 \cdot 10^{-8}$ m/s, whereas the matrix permeability from the site-scale model corresponds to a hydraulic conductivity of only $4 \cdot 10^{-11}$ m/s. The ponded boundary condition applied during the experiment (~7 cm of water) precludes a large pressure increase from occurring. Therefore, it appears that the permeability of the rock around the LPZ injection interval is actually significantly greater than the site-scale model value, which comes from core-sample measurements [*Flint*, 1996]. This finding is consistent with air-permeability tests conducted in boreholes at the fracture-matrix interaction test site (Figure 4), which all yield permeabilities of at least $3 \cdot 10^{-14}$ m^2, even in test intervals not intersecting explicitly modeled fractures. This permeability is four orders of magnitude larger than the permeabilities determined from core-sample measurements.

Modified Model

We hypothesize that the larger permeability characterizes a network of small fractures and cracks that either do not extend to the alcove wall or are too small to be included in the fracture mapping there. We denote this as the secondary fracture network and assume that it is characterized by less permeable, less extensive fractures than those making up the primary (mapped) fracture network. We do not attempt to resolve individual features of the secondary fracture network explicitly in the model. As discussed in *Salve et al.* [this issue], the significant decline in flow rate observed during the constant-head portions of the LPZ tests suggests a strongly heterogeneous medium, such as a fracture network comprising a range of fracture sizes, which would probably require finer spatial discretization than the present model has. Rather, we treat the secondary fracture network as an effective continuum by assigning to the matrix gridblocks a permeability of $5 \cdot 10^{-15}$ m^2, consistent with the injection rates observed during the latter portions of the LPZ tests. To accompany this thousand-fold increase in permeability, we decrease capillary pressure strength by a factor of 30 (following the commonly used *Leverett* [1941] relationship $P_{cap} \sim k^{-1/2}$).

Assignment of initial saturation conditions is improved by fitting an analytical expression to the observed P_{cap} values shown in Figure 7:

$$P_{cap}(y) = -430e^{y}, \qquad (7)$$

with y and P_{cap} in meters. We then invert the *van Genuchten* [1980] $P_{cap}(S)$ expression to produce $S(P_{cap}(y)) = S(y)$. This procedure yields an initial saturation at the LPZ of 0.31.

Finally, we set the porosity of the secondary fracture network to 3%. As described below, this value is needed for the model to reproduce the capillary pressure changes at the locations of observation boreholes C and D. It suggests a hierarchical structure in which there is less primary fracture volume and more secondary fracture volume. Table 4 summarizes the model changes made for the LPZ tests.

Modeled Saturation Changes

The three LPZ tests can be successfully simulated with the modified model, in that water can be injected without pressures building up much higher than atmospheric pressure and no water breaks through at the slot. With 2% porosity, the model yields capillary pressure changes at the locations of the observation boreholes that occur too quickly and are too big compared to field observations. With 4% porosity, modeled changes are too gradual and small. With 3% porosity, the modeled response, shown in Figure 8a, agrees qualitatively with field observations between 1 and 1.5 m from the borehole collar, where the maximum changes in capillary pressure occur [*Salve et al.*, this issue, Figure 7b and d]. Modeled responses at the locations of the two observation boreholes are similar and are combined in one profile in Figure 8a. The modeled capillary pressure increases relatively quickly after the start of test LPZ-1, but decreases much more gradually after the test ends and has not decreased significantly by the time test LPZ-3 begins. The field observations show a similar initial increase, but a more dynamic response between LPZ-2

and LPZ-3, especially in borehole D. Additionally, field data show significant responses more than 2 m from the borehole collar, whereas the modeled response becomes negligible at 1.7 m.

Figure 9 shows the modeled saturation distribution at a series of times during the LPZ tests. The plume of injected water spreads in all directions away from the injection interval, as capillary forces play a stronger role than gravity for the relatively low permeability of the secondary fracture network. The final conditions after the rest period following test LPZ-3 become the initial conditions for the first HPZ test.

4.2. HPZ Tests

Alternative Conceptual Models

Air-permeability measurements suggest that the secondary fracture network is widespread. However, air permeability does not provide a direct prediction of liquid permeability, and the LPZ injection interval is the only location where water was released away from a primary fracture. Therefore, we develop two alternative models for the HPZ tests, one in which the secondary fracture network properties are assigned to all matrix gridblocks (Case A), and the other in which they are assigned only to matrix gridblocks in the vicinity of the LPZ, with UZ site-scale model properties maintained elsewhere (Case B). The two models yield similar results for the LPZ tests, but differ greatly for the HPZ tests, as discussed below.

The vertical fracture permeability used in the UZ site-scale model, $7 \cdot 10^{-12}$ m^2, agrees well with both the air-permeability value obtained for the HPZ ($6.8 \cdot 10^{-12}$ m^2) and the hydraulic conductivity inferred from the constant-head tests HPZ-1 and HPZ-2 ($4 \cdot 10^{-12}$ and $3 \cdot 10^{-12}$ m^2, respectively). Therefore, the fracture permeabilities shown in Table 3 are not modified for the simulations of the HPZ tests. However, because of the large contrast between fracture and matrix permeabilities, care must be taken for the numerical model to calculate fracture-matrix flow correctly. By default, TOUGH2 uses upstream weighting for the permeability at the interface between two elements, which means that during the liquid-release tests, the large fracture permeability would control flow out of the fractures into the surrounding matrix. We can avoid this effect by requiring that the lower matrix permeability be used at fracture-matrix interfaces.

To further investigate the nature of fracture-matrix interactions, we also simulate the HPZ tests with two other models. Case B1 is just like Case B except that upstream weighting is used for the permeability at fracture-matrix interfaces, making the potential for fracture-matrix flow much greater than for Case B. However, this flow does not spread throughout the matrix elements, because for matrix-to-matrix connections, permeability is still the low site-scale model value. Hence, the model simulates a relatively large flow out of the primary fracture network that remains localized around the fractures. This may be considered to represent flow into a region with properties intermediate between those of the primary fractures and the matrix, consisting of small or dead-end fractures, or highly distressed matrix. Unlike the secondary fracture network of Case A, which extends everywhere the primary fracture network is not, here the increased permeability

region forms a narrow shell around the primary fractures. Case C considers the fracture network only, with all matrix elements removed from the grid. To simplify the discussion in the remainder of the paper, we generally refer to the portion of the model that is not part of the primary fracture network as "the matrix", regardless of whether it represents the secondary fracture network, the increased permeability shell, or the site-scale model matrix.

As described in Section 3.1, fracture porosities in the range of 0.1% to 4% have been estimated in previous ESF studies. We used 1% for the preliminary scoping studies, but reduce the value used for the primary fracture network to 0.5% to model the HPZ tests, to better match the short breakthrough times obtained for large liquid-release rates.

Modeled Saturation Changes

As an illustration of the general response to the HPZ tests, Figure 10 shows snapshots of the liquid saturation distribution during the tests for Case A. In contrast to the LPZ tests, here gravity-driven vertical flow dominates. Saturations in the fractures underlying the injection interval increase quickly after the start of each test and decrease quickly after the end of each test, whereas outlying fracture and matrix saturations change more gradually. During each test, much of the injected water travels straight downward through Fracture 10 and breaks through into the slot below the injection interval, as was observed in the field.

Figures 8b-d show the modeled capillary pressure responses to the HPZ tests in matrix gridblocks corresponding to monitoring locations in the observation boreholes, for Cases A, B, and B1. Case A responses tend to be largest, and extend farthest from the injection interval, whereas Case B responses are extremely small and limited to the immediate vicinity of the injection interval. The field data [*Salve et al.*, this issue, Figure 8] show a variety of responses, with some locations better modeled by Case A and others by Case B1. Such a varied response suggests a heterogeneous matrix, in which the secondary fracture network, while widespread, does not uniformly fill all of the space.

Seepage into Slot

In Figure 11, breakthrough time at the slot, t_{bt}, and the fraction of injected water captured by the slot, M_{slot}/M_{inj}, are compared to the values observed in the field for all the HPZ tests. The analytical solution for t_{bt} assuming purely gravity-driven flow, Equation (5), and the corresponding value of M_{slot}/M_{inj} in which all injected water eventually reaches the slot are also shown. Generally, the results for Case C (the no-matrix case) and Case B (the site-scale matrix case) are very similar, indicating that with the site-scale model properties, the matrix plays only a small role in the HPZ test responses. Overall, results for Case A (secondary fracture network) and Case B1 (increased permeability shell), in which flow is not confined to the primary fractures, compare more favorably to the field data. Comparisons of specific features of the field data and model results shown in Figure 11 are described in the following two sub-sections.

Breakthrough Time

We interpret the t_{bt} variation between tests as arising from a combination of two opposing influences. First, as injection rate decreases, t_{bt} increases because $k_{rlf}(S_{lf})$ decreases, in accordance with the analytical solution. In fact, the increase is even greater than predicted by Equation (5) because lateral flow and fracture-matrix interactions (t_{bt} lengthening effects not accounted for in the analytical solution) become more effective as injection rate decreases. Second, with several liquid-release tests closely spaced in time, each showing a significant fraction of the injected water remaining in the formation, the initial saturation around the injection interval is likely to vary from test to test (the so-called history or memory effect). The single-fracture model discussed in Section 3.2 indicated that for an idealized homogeneous fracture, t_{bt} decreases as initial saturation increases. For a more realistic heterogeneous fracture network, we expect that remaining water will preferentially occupy smaller, low-permeability, or dead-end fractures because of capillary effects, eliminating them from the active flow path for subsequent liquid-release tests and further decreasing t_{bt}.

The history effect is not included in the analytical solution, which assumes that initial saturation is near residual saturation, so t_{bt} steadily increases as q_{inj} decreases (Figure 11). However, both the observed data and the numerical model show a decrease in t_{bt} between tests HPZ-1 and HPZ-2 despite a small decrease in q_{inj}, and the observed data show no increase in t_{bt} between tests HPZ-2 and HPZ-3 when q_{inj} is decreased considerably. That the history effect is not apparent in the observed data between tests HPZ-5 and HPZ-6

suggests that low-permeability components of the system remain saturated prior to HPZ-5, almost three weeks after the conclusion of HPZ-4.

Figure 11 also indicates that for all but the lowest injection rates (HPZ-4 and HPZ-8), numerically modeled breakthrough times are generally too long. We can isolate the effect of fracture-matrix flow by comparing t_{bt} for Cases B and C, in which the matrix plays almost no role, with t_{bt} for Cases A and B1. Breakthrough time is longer for all HPZ tests when fracture-matrix flow is present, but for later tests the difference is smaller because the region surrounding the fracture is already wet at test start, decreasing imbibition away from the fracture fast flow path. We conjecture that for medium and high injection rates, fracture heterogeneity allows some pure vertical gravity-dominated flow to occur, while other fracture flow paths spread laterally within the fracture and interact more with the surrounding matrix. Hence, the analytical solution and no-matrix models are better predictors of t_{bt}. For low injection rates, capillarity becomes relatively more important for all fracture flow paths and a gravity-dominated t_{bt} is not observed. Similarly, fracture-matrix flow becomes relatively more important, making t_{bt} for the no-matrix cases much too short. For test HPZ-4, with the lowest injection rate, fracture-matrix flow is such a big factor that only Case A (with a widespread secondary fracture network that can imbibe a large fraction of the injected water) produces a reasonable value of t_{bt}.

Because the HPZ tests were conducted using different injection rates, they illustrate how t_{bt} is inversely related to q_{inj} (although the picture is complicated by history effects). We

can use the 3-D fracture-network model to examine the sensitivity of t_{bt} to fracture properties such as ϕ_f and k_f. Equation (5) predicts that for 1-D gravity flow, t_{bt} is directly proportional to ϕ_f and inversely proportional to k_f. As ϕ_f is decreased in the numerical model, t_{bt} does get shorter, but the dependence is not nearly as strong as in the analytical solution. The weaker dependence occurs because as ϕ_f decreases, a much greater fraction of the injected water can be imbibed into the matrix, delaying t_{bt}. As k_f is increased in the numerical model, t_{bt} also gets shorter, but again the dependence is not as strong as in the analytical solution. For as k_f increases, in-fracture spreading also increases, which tends to lengthen t_{bt}.

Mass Recovery

We interpret the variation of M_{slot}/M_{inj} between tests as arising from two distinct effects. First, M_{slot}/M_{inj} tends to be inversely related to t_{bt}, as slower gravity flow allows more time for capillary-driven flow (matrix imbibition and lateral spreading and trapping in the fracture) to occur. Second, M_{slot}/M_{inj} tends to increase as the saturation surrounding the primary flow path increases and the driving forces for capillary flow diminish.

In the field data, the general trends expected for t_{bt} and M_{slot}/M_{inj} are intertwined with the effects of flow-path heterogeneities, which may be quite strong. For example, we nominally expect that (without history effects) decreasing q_{inj} increases t_{bt} and decreases M_{slot}/M_{inj}. However, if decreasing q_{inj} left saturation of the main preferential flow path unchanged while eliminating other slower flow paths, it could yield no change in t_{bt} and an increase in M_{slot}/M_{inj}.

Figure 11 shows that values of M_{slot}/M_{inj} for the no-matrix cases (B and C) are much larger than the observed ones, suggesting that flow out of the primary fractures does in fact account for some of the water not reaching the slot. For Case B1, with an increased permeability shell around the fractures, M_{slot}/M_{inj} is smaller, but still too big. Notably, the decrease in M_{slot}/M_{inj} from Case B to Case B1 is largest for the first test. Once the shell wets up, it no longer effectively imbibes water from the fracture. Overall, Case A matches the observed values of M_{slot}/M_{inj} best. Modeled values are too small for some HPZ tests and too big for others, and generally show the same trends as the observed values. This suggests that a widespread secondary fracture network does exist, and that what we have been calling fracture-matrix flow is largely flow between the primary and secondary fracture networks.

Figure 12 shows the cumulative fraction of injected water that is recovered at the slot as a function of injected volume for each HPZ test for Case A. The final symbol on each curve represents the fraction when slot seepage stops, which is the M_{slot}/M_{inj} value shown in Figure 11. The model results show the same general character as the field data [*Salve et al.*, this issue, Figure 9b], but much less short-term variability. As described in *Salve et al.* [this issue], unsteady seepage is a familiar feature of infiltration along heterogeneous flow paths. TOUGH2 is not capable of producing the intermittent, dripping seepage observed in the field. However, some of the variability apparent in the cumulative fraction of recovered water could be modeled by introducing heterogeneous property

distributions within the fracture network that promote multiple bifurcating and converging flow paths.

Another quantity measured during the HPZ tests is the duration and volume of seepage into the slot after injection ends. Observed seepage duration and volume range from 15 to 85 minutes and 0.5 to 1.3 L, respectively, for the various HPZ tests. Both Cases A and B1 predict about the right duration of seepage (19 to 90 minutes), but underpredict the volume (0.2 to 0.5 L), suggesting that the modeled flow path volume is too small. Increasing fracture porosity would increase flow-path volume, but would make breakthrough times too long. What is needed instead is a heterogeneous fracture model, in which permeability and porosity vary spatially. Such a model would promote channelized flow, in which fast flow paths yield short breakthrough times and slow flow paths increase post-test seepage.

5. Summary and Conclusions

We have developed and applied a 3-D quasi-explicit fracture-network model to a series of liquid-release tests in Alcove 6 of the ESF at Yucca Mountain, Nevada. Fractures are modeled with relatively large gridblocks using fracture-continuum properties, but unlike most such models, fracture gridblocks are located deterministically rather than stochastically, enabling fracture connectivity to be preserved. Connectivity is critical for modeling liquid flow at this scale, where fracture spacing is comparable to the distances between the injection interval, the observation boreholes, and the slot.

Before using the fracture-network model, we used preliminary analytical and numerical scoping studies to illustrate key aspects of the problem, including isolation of gravity-driven flow through a vertical fracture and the subsequent addition of lateral spreading within the fracture plane, history effects, and fracture-matrix flow. Simulations with the fracture-network model yield reasonably good matches to the basic results of the liquid-release tests: t_{bt}, breakthrough time at the slot, the M_{slot}/M_{inj}, the fraction of injected water that is captured by the slot, and temporal variations of capillary pressure measurements made at observation boreholes.

A key finding of this work concerns the nature of the fracture network in the welded tuff at the test site. It has become common practice to conceptualize the fractured tuffs at Yucca Mountain as consisting of high-permeability fractures embedded in a very low-permeability rock matrix. This conceptualization does not work well for the liquid-release tests conducted at the fracture-matrix interaction test site in Alcove 6. We find that a model containing two fracture networks with different characteristics works much better to explain the observed data. In this model, much of the flow occurs quickly through the primary fracture network, (fractures large enough and extensive enough to be mapped on the alcove walls and ceiling). However, a secondary fracture network also exists, consisting of lower-permeability, less-continuous fractures that span a range of sizes. With such a network, the LPZ tests can accept a large volume of water without showing breakthrough at the slot, and the HPZ tests show a lower fraction of water recovered at the slot than can be explained by imbibition into an intact rock matrix.

Moreover, it appears that while the secondary fracture network is not just localized around the primary fractures, neither does it uniformly pervade the rock.

An assessment of the tools developed for this study leads to the following conclusions:

(1) Analytical solutions provide an excellent tool for experimental design, especially when simple enough to be incorporated into a spreadsheet format, but they are not sophisticated enough to reproduce all the features of field behavior that the numerical models can. The 1-D analytical solution assuming pure gravity flow gives a lower limit for the breakthrough time of an isolated liquid-release test, which can be lengthened by lateral flow within the fracture and fracture-matrix flow. In contrast, history effects can shorten breakthrough time compared to the analytical solution.

(2) The numerical quasi-explicit fracture-network model created with the mesh generator FRACGRID, although very simple, does a remarkably good job of capturing many of the features of the real liquid-release test. It provides a useful tool for experimental design and experiment interpretation. In particular, it has proved valuable for site characterization, using observed data to infer model parameters.

(3) The overprediction of t_{bt}, and the underprediction of post-test seepage by the fracture-network model indicate the need to incorporate heterogeneity within the primary fractures. This can be readily accomplished within the present FRACGRID framework.

(4) We need to continue to investigate the impact of using different conceptual and mathematical treatments for transient fracture-matrix interactions. To resolve the steep gradients accompanying transient fracture-matrix flow, it may be feasible to use the FRACGRID mesh generator as a first step, then further subdivide fracture gridblocks to provide fine resolution of the material adjacent to the primary fracture network. Another potential improvement would be to represent the secondary fracture network with a dual continuum model, consisting of both fracture and matrix continua, rather than with the present effective continuum model, which essentially ignores the matrix.

Acknowledgments

The careful reviews of this paper by H.H. Liu, Peter Persoff, and Dan Hawkes are greatly appreciated. We thank Jerry Fairley for fruitful discussions on conceptual model development. This work was supported by the Director, Office of Civilian Radioactive Waste Management, U.S. Department of Energy, through Memorandum Purchase Order EA9013MC5X between TRW Environmental Safety Systems, Inc. and the Ernest Orlando Lawrence Berkeley National Laboratory, through the U.S. Department of Energy Contract No. DE-AC03-76SF00098.

References

Barenblatt, G. E., I. P. Zheltov, and I. N. Kochina, Basic concepts in the theory of homogeneous liquids in fissured rocks, *J. Applied Mathematics* (USSR), *24*(5), 1286–1303, 1960.

Beason, S. C., Geologic mapping of the ESF: ESF—Main Drift, Alcove 6 as-built geology and geotechnical data, Drawing OA-46-303, Yucca Mountain Project, U.S. Geol. Survey, 1997.

Birkholzer, J. T. and Y. W. Tsang, Pretest analysis of the thermal-hydrological conditions of the ESF drift scale test, *Rep. LBNL-41044*, Lawrence Berkeley National Laboratory, Berkeley, CA, 1997.

Birkholzer, J., G. Li, C. -F. Tsang, and Y. Tsang, Modeling studies and analysis of seepage into drifts at Yucca Mountain, *J. of Contaminant Hydrology*, *38*(1–3), 349–384, 1999.

Doughty, C., Investigation of conceptual and numerical approaches for evaluating moisture, gas, chemical and heat transport, *J. of Contaminant Hydrology, 38*(1–3), 69–106, 1999a.

Doughty, C., Mathematical modeling of a ponded infiltration test in unsaturated fractured basalt at Box Canyon, Idaho, *Rep. LBNL-40630*, Lawrence Berkeley National Laboratory, Berkeley, CA, 1999b.

Doughty, C., Numerical model of water flow in a fractured basalt vadose zone: Box Canyon site, Idaho, *Water Resour. Res.*, in press, 2000.

Edwards, A. L., TRUMP: A computer program for transient and steady state temperature distributions in multidimensional systems, National Technical Information Service, National Bureau of Standards, Springfield, VA, 1972.

Flint, L., Matrix properties of hydrogeologic units at Yucca Mountain, Nevada, U.S. Geological Survey report (draft), U.S. Geological Survey, Denver, CO, 1996.

Freifeld, B. and Y. W. Tsang, Active hydrogeological testing, In second quarter TDIF submission for the drift scale test (hydrological, radar, microseismic), Chapter 2, *Yucca Mountain Project Level 4 Milestone Report SP2790M4*, Lawrence Berkeley National Laboratory, Berkeley, CA, 1998.

Leverett, M. C., Capillary behavior in porous solids, *Trans. Soc. Pet. Eng. AIME, 142*, 152-169, 1941.

McLaren, R. G., P.A. Forsyth, E. A. Sudicky, J. E. VanderKwaak, F. W. Schwartz, and J. H. Kessler, Flow and transport in fractured tuff at Yucca Mountain: numerical experiments on fast preferential flow mechanisms, *J. Contaminant Hydrology*, *43*(3–4), 211–238, 2000.

Moridis, G. and K. Pruess, TOUGH simulations of Updegraff's set of fluid and heat flow problems, *Rep. LBL-32611*, Lawrence Berkeley Laboratory, Berkeley, CA, 1992.

Moridis, G. and K. Pruess, Flow and transport simulations using T2CG1, a package of conjugate gradient solvers for the TOUGH2 family of codes, *Rep. LBL-36235*, Lawrence Berkeley National Laboratory, Berkeley, CA, 1995.

Narasimhan, T. N. and P. A. Witherspoon, An integrated finite difference method for analyzing fluid flow in porous media, *Water Resour. Res.*, *12*(1), 57–64, 1976.

Persoff, P. and K. Pruess, Two-phase flow visualization and relative permeability measurement in natural rough-walled rock fractures, *Water Resour. Res.*, *31*(5), 1175–1186, 1995.

Philip, J. R., Numerical solution of equations of the diffusive type with diffusivity concentration dependent, *Trans. Faraday Society*, 51, 885–892, 1955.

Pruess, K., TOUGH user's guide, *Rep. LBL-20700*, Lawrence Berkeley National Laboratory, Berkeley, CA, 1987.

Pruess, K., *TOUGH2*—A general purpose numerical simulator for multiphase fluid and heat flow, *Rep. LBL-29400*, Lawrence Berkeley National Laboratory, Berkeley, CA, 1991.

Pruess, K., ed., Proceedings of the TOUGH Workshop '95, *Rep. LBL-37200*, Lawrence Berkeley National Laboratory, Berkeley, CA, 1995.

Pruess, K., ed., Proceedings of the TOUGH Workshop '98, *Rep. LBL-41995*, Lawrence Berkeley National Laboratory, Berkeley, CA, 1998.

Pruess, K. and Y. W. Tsang, On two-phase relative permeability and capillary pressure of rough-walled rock fractures, *Water Resour. Res.*, *26*(9), 1915–1926, 1990.

Pruess, K., J. S. Y. Wang, and Y. W. Tsang, On thermohydrologic conditions near high-level nuclear wastes emplaced in partially saturated fractured tuff: 1. Simulation studies with explicit consideration of fracture effects, *Water Resour. Res.*, *26*(6), 1235–1248, 1990a.

Pruess, K., J. S. Y. Wang, and Y. W. Tsang, On thermohydrologic conditions near high-level nuclear wastes emplaced in partially saturated fractured tuff: 2. Effective continuum approximation, *Water Resour. Res.*, *26*(6), 1249–1261, 1990b.

Reitsma, S. and B. H. Kueper, Laboratory measurement of capillary pressure-saturation relationships in a rock fracture, *Water Resour. Res.*, *30*(4), 865-878, 1994.

Ritcey, A. C., Y. S. Wu, E. L. Sonnenthal, C. Haukwa, and G. S. Bodvarsson, Final predictions of ambient conditions along the east-west cross drift using the 3-D UZ site-scale model, *Yucca Mountain Project Level 4 Milestone SP33ABM4*, Lawrence Berkeley National Laboratory, Berkeley, CA, 1998

Salve, R., T. K. Tokunaga, J. S. Y. Wang, R. Solbau, and J. Clyde, Hydrologic monitoring in unsaturated fractured tuff boreholes: Preliminary results, In Wang, J. S. Y., P. J. Cook, R. C. Trautz, and R. Salve, Field Testing and observation of flow paths in niches, Chapter 6, *Yucca Mountain Project Level 4 Milestone SPC314M4*, Lawrence Berkeley National Laboratory, Berkeley, CA, 1997.

Salve, R. and J. S. Y. Wang, Compilation of water potentials measured in niches, In Wang, J. S. Y., R. C. Trautz, P. J. Cook, and R. Salve, Drift seepage test and niche moisture study: Phase 1 report on flux threshold determination, air permeability distribution, and water potential measurement, Chapter 4, *Yucca Mountain Project Milestone Report SPC315M4*, Lawrence Berkeley National Laboratory, Berkeley, CA, 1998.

Salve, R., C. Doughty, J. P. Fairley, P. J. Cook, and J. S. Y. Wang, Fracture/matrix test in alcove 6, In Wang, J. S. Y. et al., Progress report on fracture flow, drift seepage and matrix imbibition tests in the Exploratory Studies Facility , Chapter 3, *Yucca Mountain Project Level 4 Milestone SP33PBM4*, Lawrence Berkeley National Laboratory, Berkeley, CA, 1998.

Salve, R., J. S.Y. Wang, and C. Doughty, Liquid flow in unsaturated fractured welded tuffs: 1. Field investigations, *Water Resour. Res.*, this issue, 2000.

Scheidegger, A. E., *The Physics of Flow through Porous Media*, 3rd ed., University of Toronto Press, Toronto, 1974.

Sonnenthal, E. L., C.F. Ahlers, and G. S. Bodvarsson, Fracture and fault properties for the UZ site-scale flow model, In G. S. Bodvarsson, T. M. Bandurraga, and Y. S. Wu, eds., The site-scale unsaturated zone model of Yucca Mountain, Nevada, for the viability assessment, Chapter 7, *Rep. LBNL-40376*, Lawrence Berkeley National Laboratory, Berkeley, CA, 1997.

Therrien, R. and E. A. Sudicky, Three-dimensional analysis of variably-saturated flow and solute transport in discretely-fractured porous media, *J. of Contaminant Hydrology*, *23*(1–2), 1–44, 1996.

Van Genuchten, M., Th. A closed-form equation for predicting the hydraulic conductivity of unsaturated soils, *Soil Sci. Soc. Amer. J.*, *44*(5), 892–898, 1980.

Vauclin, M., D. Khanji, and G. Vachaud, Experimental and numerical study of a transient, two-dimensional unsaturated-saturated water table recharge problem, *Water Resour. Res.*, *15*(5), 1089–1101, 1979.

Wang, J. S. Y., R. C. Trautz, R. Salve, C. M. Oldenburg, C. F. Ahlers, S. Finsterle, P. J. Cook, C. Doughty, J. P. Fairley, A. L. James, M. Q. Hu, M. A. Guell, and B. Freifeld, Progress report on fracture flow, drift seepage and matrix imbibition tests in the Exploratory Studies Facility, *Yucca Mountain Project Level 4 Milestone SP33PBM4*, Lawrence Berkeley National Laboratory, Berkeley, CA, 1998.

Wang, J. S. Y, R. C. Trautz, P. J. Cook, S. Finsterle, A. L. James, and J. Birkholzer, Field tests and model analyses of seepage into drift, *J. of Contaminant Hydrology, 38*(1–3), 323–347, 1999.

Warren, J. E. and P. J. Root, The behavior of naturally fractured reservoirs, *Soc. Pet. Eng. J, 228*, 245–255, 1963.

Wu, Y. S., C. F. Ahlers, P. Fraser, A. Simmons, and K. Pruess, Software qualification of selected TOUGH2 modules, *Rep. LBNL-39490*, Lawrence Berkeley National Laboratory, Berkeley, CA, 1996.

Wu, Y. S., C. Haukwa, and G. S. Bodvarsson, A site-scale model for fluid and heat flow in the unsaturated zone of Yucca Mountain, Nevada, *J. of Contaminant Hydrology, 38*(1-3), 185–215, 1999.

Zimmerman, R. W. and G. S. Bodvarsson, An approximate solution for one-dimensional absorption in unsaturated porous media, *Water Resour. Res., 25*(6), 1422–1428, 1989.

Tables

Table 1. Fracture geometry data used for the FRACGRID mesh generator.

Fracture ID number	Strike (degrees from north)	Dip (degrees from horizontal)	Reference x coordinate* (m)	Center coordinates (x, y in m)	Radius (m)
3	219	+73	58.32		100[a]
4	218	-77	58.72		100
5	211	+70	58.85		100
6	158	+78	54.53		100
7	172	+82	57.03	57.2, –1	1.5
8	151	+69	57.50		100
9	140	-80	56.79		100
10	124[b]	90	55.20		100
11	119	-83	56.00		100
12	129	-78	58.20	58.5, 0	1
15	145	-70	56.45	57.2, –0.5	1.5
16	341	+14	55.80	55.8, –0.5	1
17	118	+07	58.20	60.4, –0.5	1
18	197	+58	59.55		100
19	131	-76	59.20	59.2, 0	0.75
20	131	+38	52.80		100
21	127	-84	51.10		100

*All fractures have reference values of $y = 0$ and $z = 1.125$ m.

[a]A radius of 100 m is effectively infinite as the model is less than 4 m on a side; for an infinite radius, the center coordinate is not used.

[b]After construction of a preliminary 3-D model and comparison with air-permeability measurements in the injection borehole, this strike was changed to 152.

Table 2. Breakthrough time t_{bt} in minutes, calculated by Equation (5). S_{lf} is shown in parenthesis.

q_{inj}	k_f (m^2)			
(ml/min)	**10^{-11}**	**10^{-12}**	**10^{-13}**	**10^{-14}**
100	6.62 (0.85)	26.7 (1)	267 (1)	2670 (1)
50	11.4 (0.73)	26.7 (1)	267 (1)	2670 (1)
10	38.7 (0.50)	66.2 (0.85)	267 (1)	2670 (1)
5	65.0 (0.42)	114 (0.73)	267 (1)	2670 (1)

Table 3. Material properties, initial conditions, and boundary conditions for the single-fracture with matrix model and the fracture-network models.

Fracture Properties	**Value**	**Justification**
Horizontal permeability*	$4.27 \cdot 10^{-13}$ m^2	UZ site-scale model†
Vertical permeability*	$6.76 \cdot 10^{-12}$ m^2	UZ site-scale model
Porosity	0.005 – 0.01[a]	Gas-phase tracer tests[b], niche study water arrival times[c]
Van Genuchten α_f	10^{-3} Pa^{-1}	ESF fracture map analysis[d]
Van Genuchten m_f	0.63	ESF fracture map analysis
Residual liquid saturation	0.01	UZ site-scale model
Matrix Properties	**Value**	**Justification**
Horizontal permeability	$4.07 \cdot 10^{-18}$ m^2	UZ site-scale model
Vertical permeability	$4.07 \cdot 10^{-18}$ m^2	UZ site-scale model
Porosity	0.089	UZ site-scale model
Van Genuchten α_m	10^{-6} Pa^{-1}	UZ site-scale model
Van Genuchten m_m	0.32	UZ site-scale model
Residual liquid saturation	0.18	UZ site-scale model
Initial Conditions	**Value**	**Justification**
Fracture saturation	0.045	Adjusted to produce reasonable natural-state percolation rate
Matrix saturation	0.928	UZ site-scale model
Boundary Conditions	**Feature**	**Justification**

Water injection interval	Constant-rate mass source	Approximates experimental conditions
Slot	Constant-property boundary, $P_{cap} = 0$	Expect relative humidity at slot ceiling is close to one
Top and sides of model	Closed boundary	Mesh designed so water flow does not reach sides or top
Bottom of model	Constant-property boundary, usual P_{cap}	Allows water that flows around slot to leave model

*For 3-D model, fracture intersections assigned five times permeability of individual fractures

†UZ site-scale model properties are for the middle nonlithophysal zone of the TSw [*Ritcey et al.*, 1998]

[a]Preliminary scoping studies use 0.01, 3-D model uses 0.005.

[b]*Freifeld and Tsang* [1998]

[c]*Salve et al.* [1998]; *Wang et al.* [1999]

[d] *Sonnenthal et al.* [1997]

Table 4. Model modifications to convert matrix properties to secondary fracture network properties, made to match field observations during the LPZ tests.

Parameter	Original value	Modified value	Reason
Permeability	$4 \cdot 10^{-18}$ m^2	$5 \cdot 10^{-15}$ m^2	Match observed injection rate and air-permeability values
Porosity	0.089	0.03	Match P_{cap} observations
van Genuchten α_m	10^{-6} Pa^{-1}	$3 \cdot 10^{-5}$ Pa^{-1}	Scale P_{cap} with permeability
Initial saturation	0.928	$S(P_{cap})$ with $P_{cap}(y)$ from Figure 7	Match pre-test P_{cap} distribution

Figure Captions

Figure 1. Conceptualization of the quasi-explicit fracture-network model: (a) including matrix elements, fracture elements, and elements representing the intersection of the two fractures; (b) excluding matrix elements.

Figure 2. As-built geology and geotechnical data [*Beason*, 1997] showing the fracture pattern observed on the walls and ceiling of Alcove 6 around the fracture-matrix interaction test site. The horizontal axis (x) shows the distance from the ESF and the vertical axis (z) shows the height above the alcove floor, both in meters. The model uses fractures mapped between x = 0+52 and 0+61, and from the base right wall to the right springline (SPL).

Figure 3. The preliminary 3-D fracture-network model of the fracture-matrix interaction test site, constructed using only fracture geometry mapped at the alcove wall. The cut-away view shows the plane of injection borehole A and the surface just above the top of the slot. Liquid-release intervals in the HPZ (y • –2 m) and LPZ (y • –1 m) are also shown. Fracture ID numbers correspond to values in Table 1.

Figure 4. Air-permeability measurements made in the three boreholes overlying the slot at the fracture-matrix interaction test site [*Salve et al.*, 1998]. Large symbols identify inferred locations where the boreholes intersect Fracture 10.

Figure 5. The modified 3-D fracture-network model of the fracture-matrix interaction test site, constructed using air-permeability profiles to constrain the Fracture 10 location.

Figure 6. Results of the single fracture with matrix model for an injection rate of 6 ml/min using the parameters given in Table 3.

Figure 7. Observed capillary pressure as a function of distance from niche and alcove walls in the ESF under quiescent conditions [*Salve and Wang*, 1998]. P_{cap} values are converted to liquid saturations and used as initial conditions for the first LPZ liquid-release test.

Figure 8. Modeled capillary pressure responses to liquid-release tests at observation borehole locations: (a) LPZ tests; (b)-(d) HPZ tests. In each case, modeled responses at the locations of boreholes C and D are similar and are combined in one profile. The injection interval and the injection periods are shown as black bars (tests LPZ-1 and LPZ-2 are combined in one bar, as are tests HPZ-1 through HPZ-4 and tests HPZ-5 through HPZ-8). Positive distances from the borehole collar correspond to negative y values in the 3-D model.

Figure 9. Snapshots of modeled liquid saturation distribution during the LPZ tests.

Figure 10. Snapshots of modeled liquid saturation distribution during the HPZ tests for Case A.

Figure 11. Summary of HPZ simulation results: t_{bt} is breakthrough time at the slot and M_{slot}/M_{inj} denotes the fraction of injected water captured by the slot at the end of the test. The injection rates and test schedule are also shown.

Figure 12. Modeled fraction of injected water captured by the slot, M_{slot}/M_{inj}, as a function of injected volume for the HPZ tests, Case A. Injection rate in ml/min is shown on the legend. The final symbol on each curve shows M_{slot}/M_{inj} at the cessation of seepage into the slot.

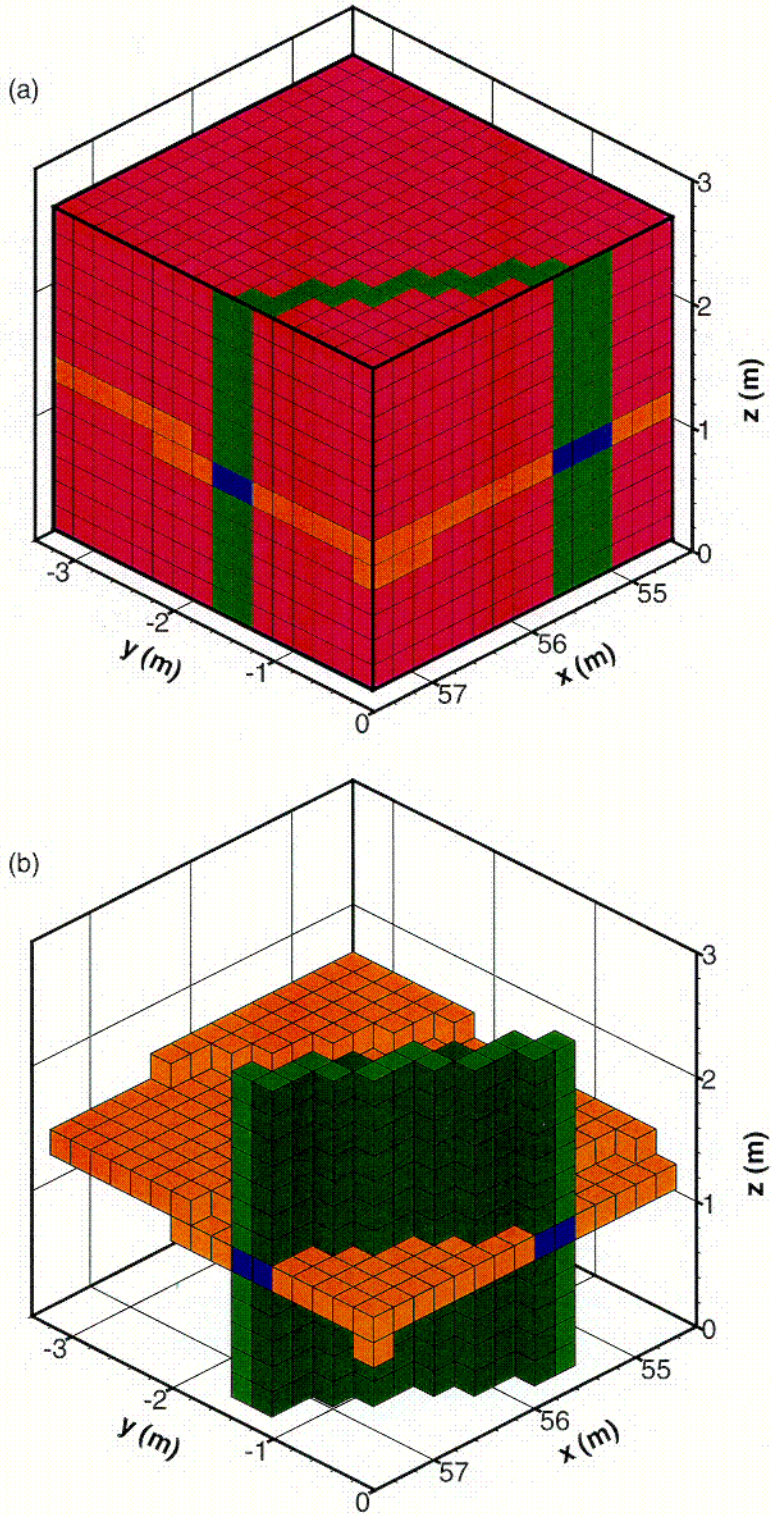

Figure 1. Conceptualization of the quasi-explicit fracture-network model: (a) including matrix elements, fracture elements, and elements representing the intersection of the two fractures; (b) excluding matrix elements.

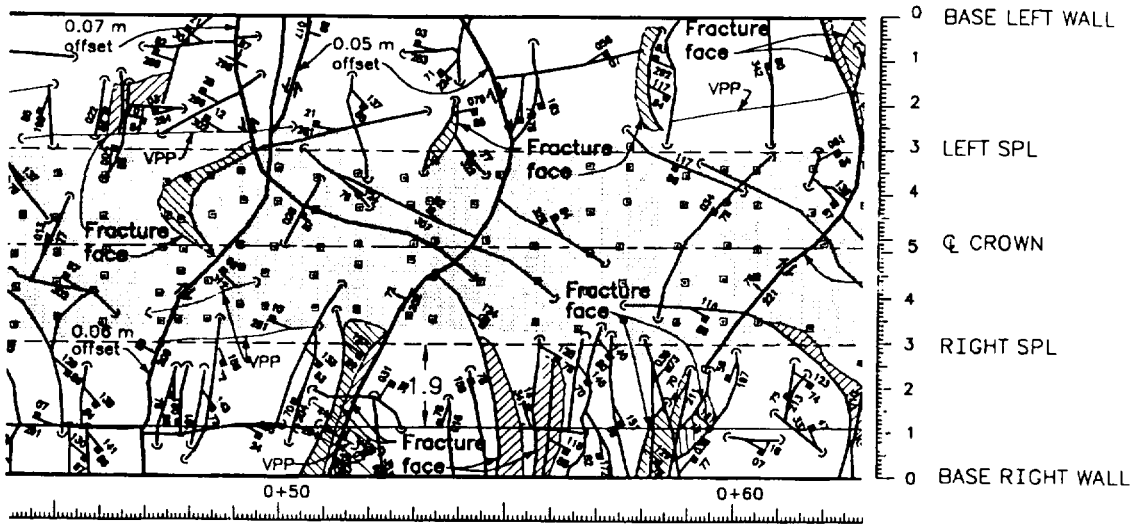

Figure 2. As-built geology and geotechnical data [*Beason*, 1997] showing the fracture pattern observed on the walls and ceiling of Alcove 6 around the fracture-matrix interaction test site. The horizontal axis (x) shows distance from the ESF and the vertical axis (z) shows height above the alcove floor, both in meters. The model uses fractures mapped between x = 0+52 and 0+61, and from the base right wall to the right springline (SPL).

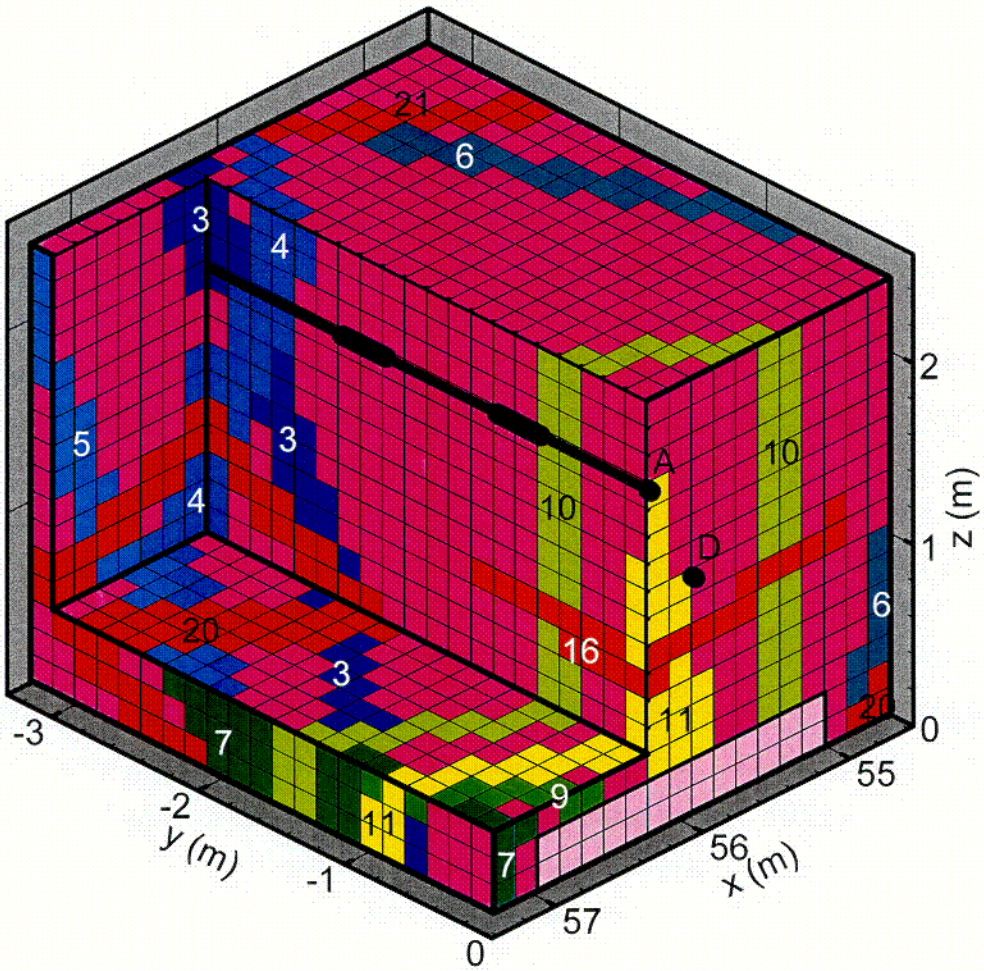

Figure 3. The preliminary 3-D fracture-network model of the fracture-matrix interaction test site, constructed using only fracture geometry mapped at the alcove wall. The cut-away view shows the plane of injection borehole A and the surface just above the top of the slot. Liquid-release intervals in the HPZ (y □ –2 m) and LPZ (y □ –1 m) are also shown. Fracture ID numbers correspond to values in Table 1.

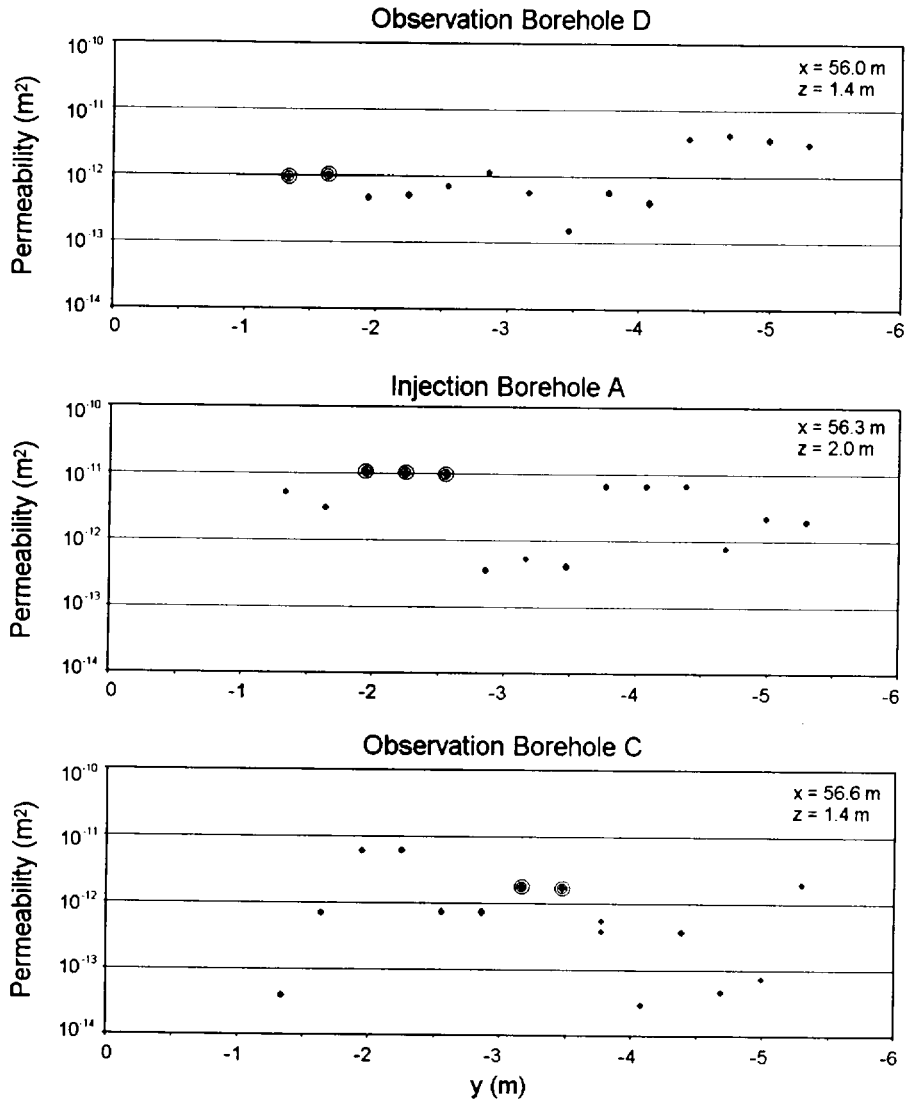

Figure 4. Air-permeability measurements made in the three boreholes overlying the slot at the fracture-matrix interaction test site [*Salve et al.*, 1998]. Large symbols identify inferred locations where the boreholes intersect Fracture 10.

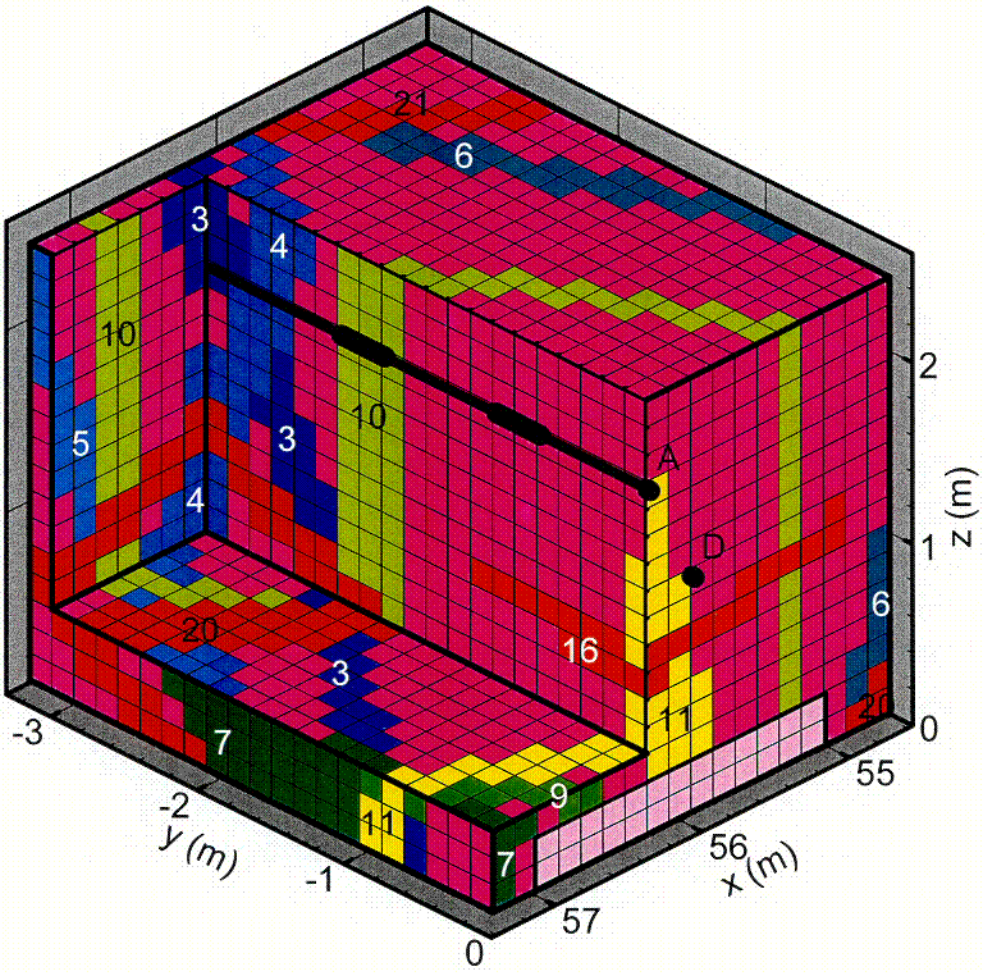

Figure 5. The modified 3-D fracture-network model of the fracture-matrix interaction test site, constructed using air-permeability profiles to constrain the Fracture 10 location.

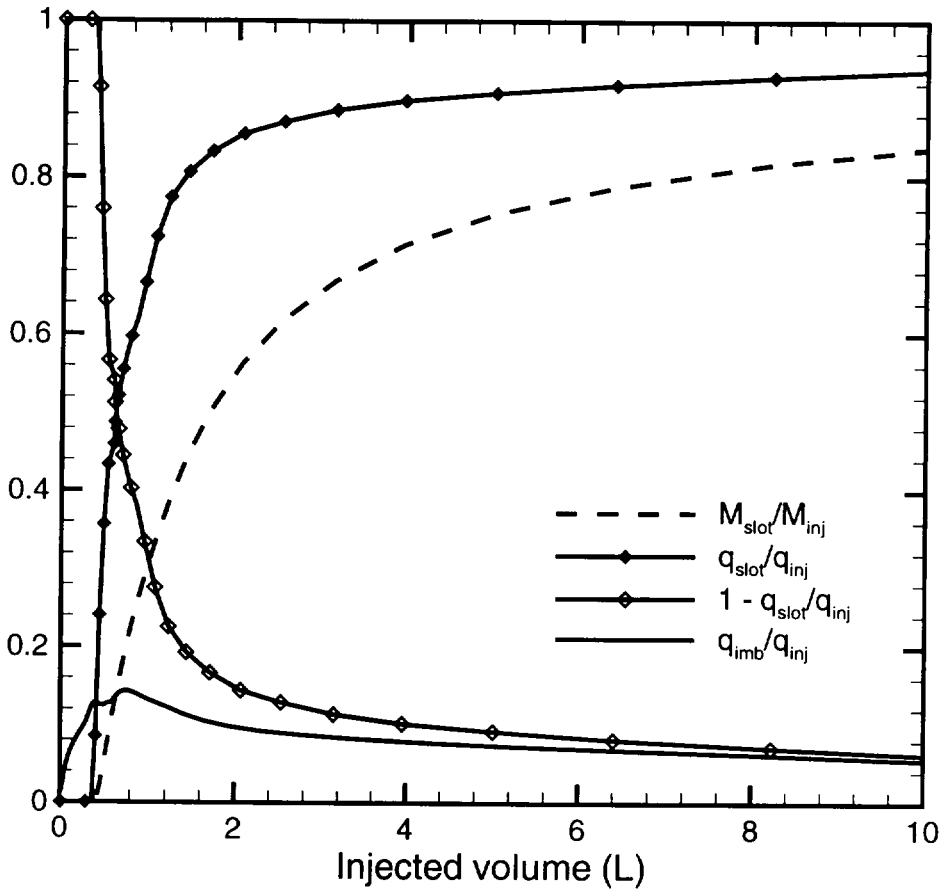

Figure 6. Results of the single fracture with matrix model for an injection rate of 6 ml/min using the parameters given in Table 3.

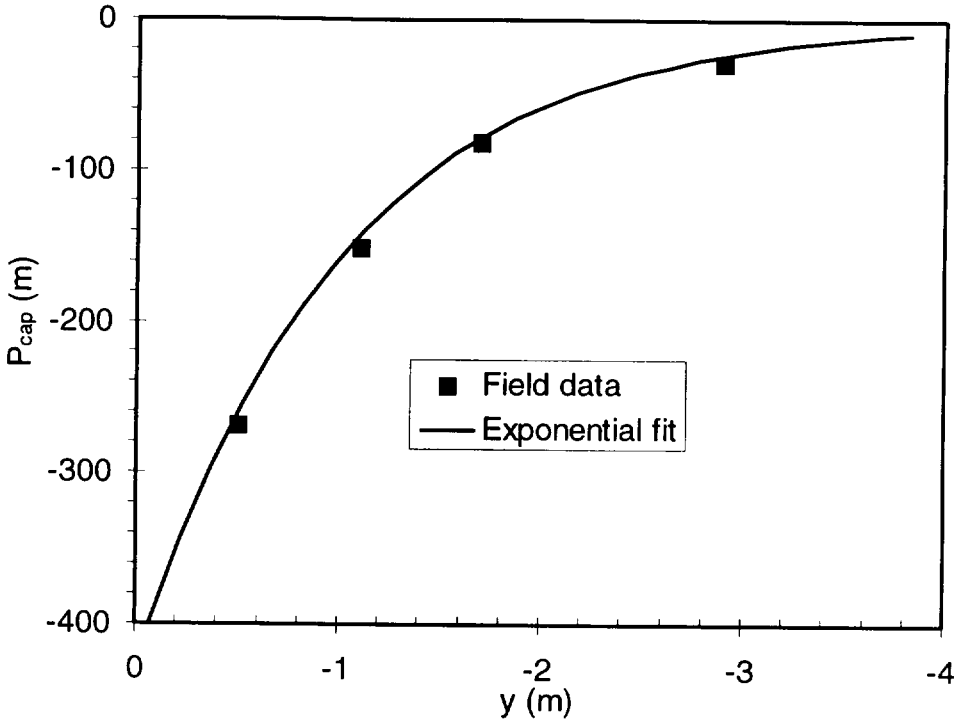

Figure 7. Observed capillary pressure as a function of distance from niche and alcove walls in the ESF under quiescent conditions [*Salve and Wang*, 1998]. P_{cap} values are converted to liquid saturations and used as initial conditions for the first LPZ liquid-release test.

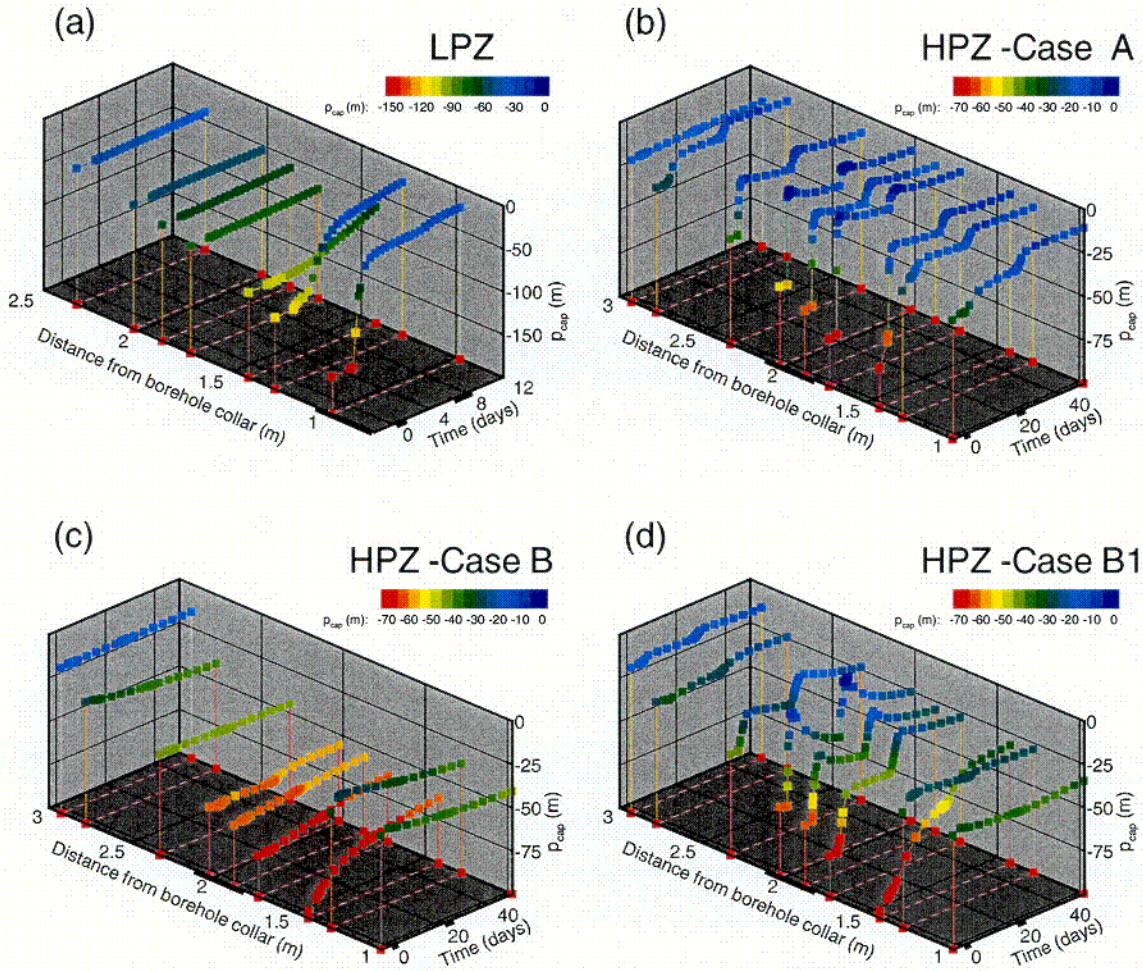

Figure 8. Modeled capillary pressure responses to liquid-release tests at observation borehole locations: (a) LPZ tests; (b)-(d) HPZ tests. In each case, modeled responses at the locations of boreholes C and D are similar and are combined in one profile. The injection interval and the injection periods are shown as black bars (tests LPZ-1 and LPZ-2 are combined in one bar, as are tests HPZ-1 through HPZ-4 and tests HPZ-5 through HPZ-8). Positive distances from the borehole collar correspond to negative *y* values in the 3-D model.

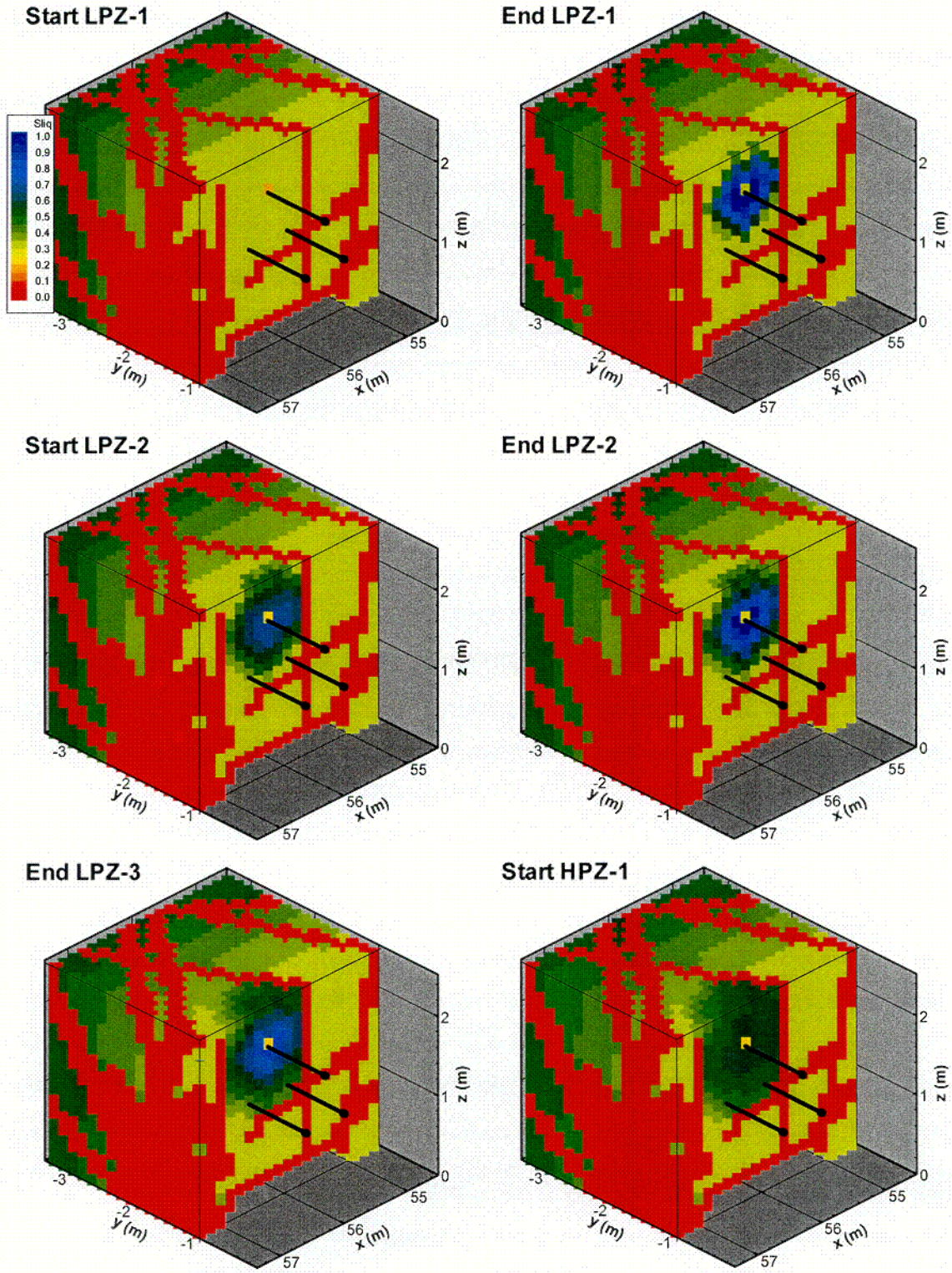

Figure 9. Snapshots of modeled liquid saturation distribution during the LPZ tests.

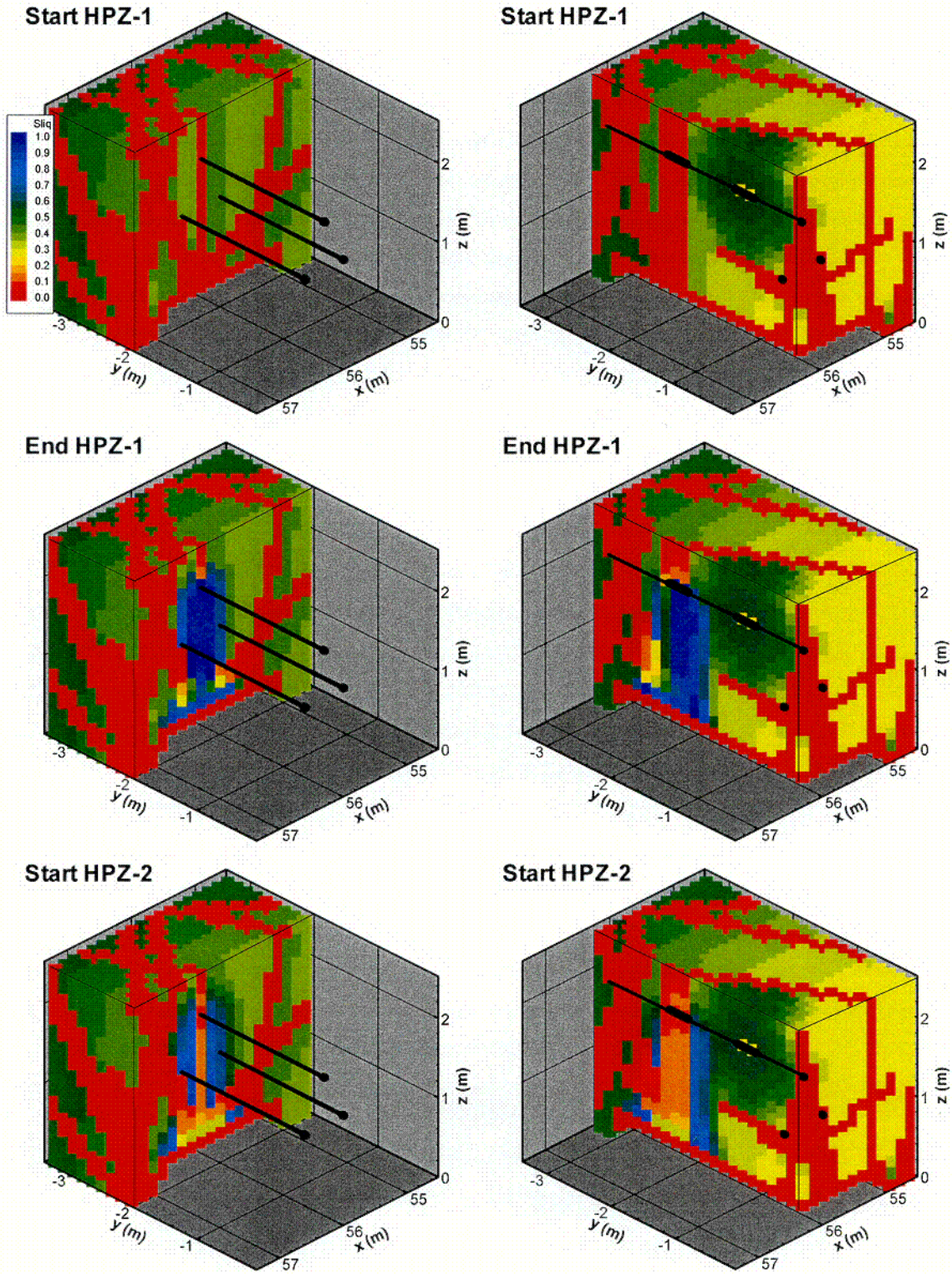

Figure 10. Snapshots of modeled liquid saturation distribution during the HPZ tests for Case A.

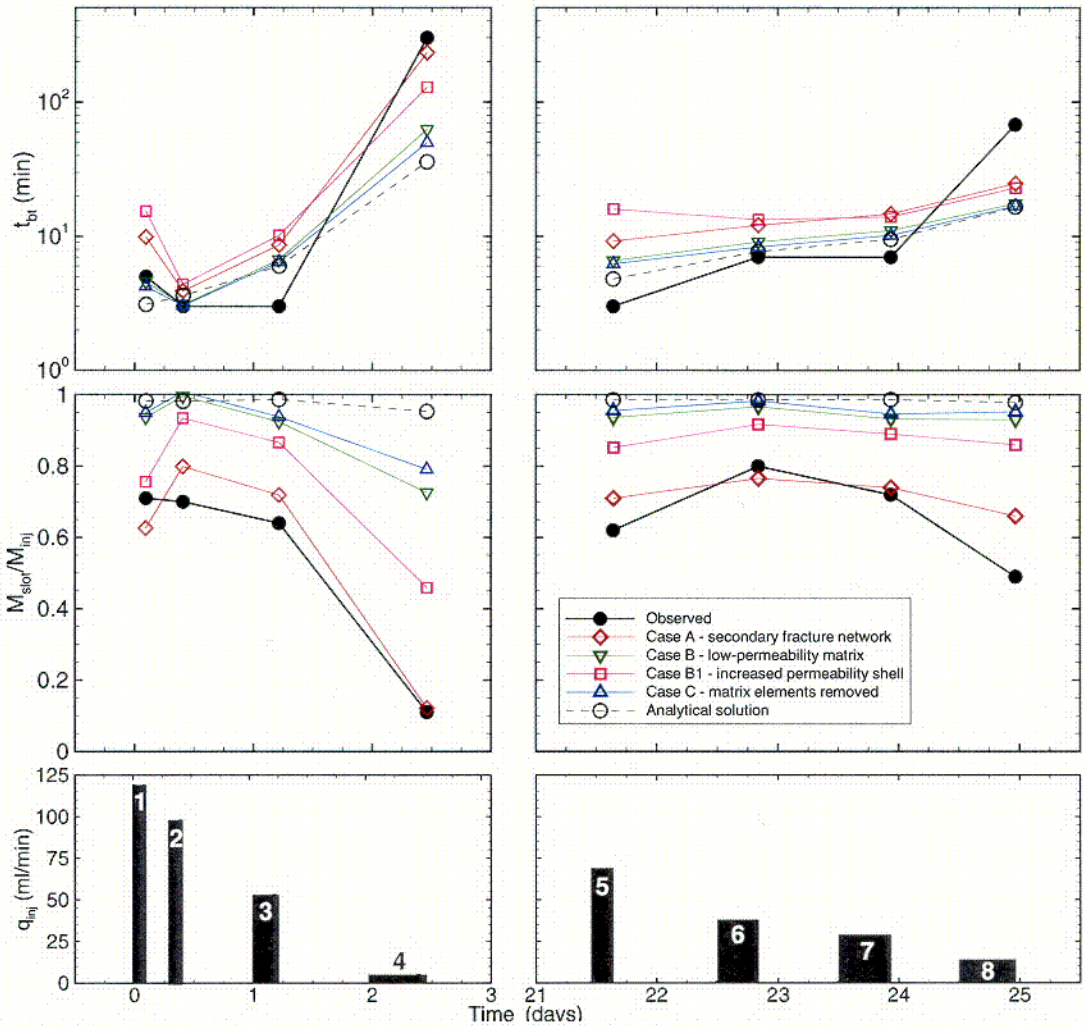

Figure 11. Summary of HPZ simulation results: t_{bt} is breakthrough time at the slot and M_{slot}/M_{inj} denotes the fraction of injected water captured by the slot at the end of the test. The injection rates and test schedule are also shown.

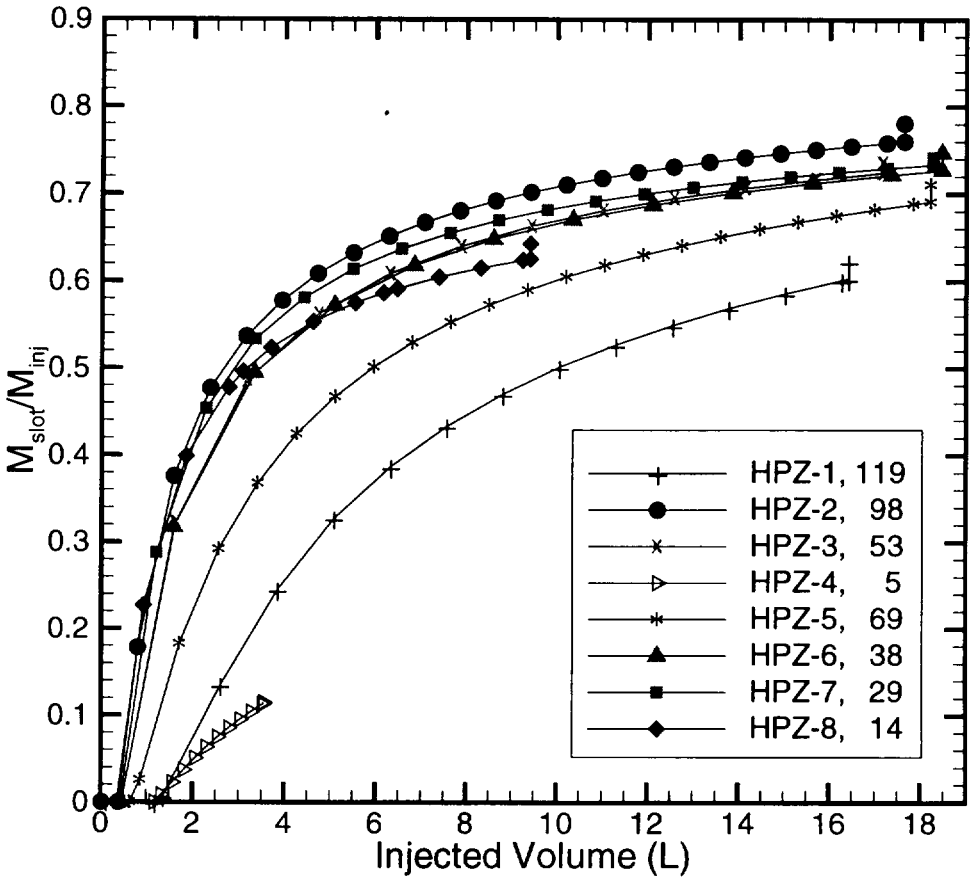

Figure 12. Modeled fraction of injected water captured by the slot, M_{slot}/M_{inj}, as a function of injected volume for the HPZ tests, Case A. Injection rate in ml/min is shown on the legend. The final symbol on each curve shows M_{slot}/M_{inj} at the cessation of seepage into the slot.